3-Deazaadenosine alleviates senescence to promote cellular fitness and cell therapy efficiency in mice

Guerrero, Ana; Innes, Andrew J.; Roux, Pierre François; Buisman, Sonja C.; Jung, Johannes; Ortet, Laura; Moiseeva, Victoria; Wagner, Verena; Robinson, Lucas; Ausema, Albertina

Published in:
Nature Aging

DOI:
10.1038/s43587-022-00279-9

Publication date:
2022

nature aging

TECHNICAL REPORT

https://doi.org/10.1038/s43587-022-00279-9

Check for updates

3-Deazaadenosine alleviates senescence to promote cellular fitness and cell therapy efficiency in mice

Ana Guerrero[1,2], Andrew J. Innes[1,2,3], Pierre-François Roux[4,5,6], Sonja C. Buisman[7], Johannes Jung[7,8], Laura Ortet[9], Victoria Moiseeva[9], Verena Wagner[1,2], Lucas Robinson[4,5,10], Albertina Ausema[7], Anna Potapova[11], Eusebio Perdiguero[9], Ellen Weersing[7], Marieke Aarts[1,2], Nadine Martin[1,2], Torsten Wuestefeld[11,12,13], Pura Muñoz-Cánoves[9,14,15], Gerald de Haan[7,16], Oliver Bischof[4,5,17] and Jesús Gil[1,2] ✉

Cellular senescence is a stable type of cell cycle arrest triggered by different stresses. As such, senescence drives age-related diseases and curbs cellular replicative potential. Here, we show that 3-deazaadenosine (3DA), an *S*-adenosyl homocysteinase inhibitor, alleviates replicative and oncogene-induced senescence. 3DA-treated senescent cells showed reduced global histone H3 lysine 36 trimethylation, an epigenetic modification that marks the bodies of actively transcribed genes. By integrating transcriptome and epigenome data, we demonstrate that 3DA treatment affects key factors of the senescence transcriptional program. Notably, 3DA treatment alleviated senescence and increased the proliferative and regenerative potential of muscle stem cells from very old mice in vitro and in vivo. Moreover, ex vivo 3DA treatment was sufficient to enhance the engraftment of human umbilical cord blood cells in immunocompromised mice. Together, our results identify 3DA as a promising drug enhancing the efficiency of cellular therapies by restraining senescence.

Senescence is a stress response that preserves tissue homeostasis by preventing the replication of old, preneoplastic or damaged cells[1]. Senescent cells undergo a stable cell-cycle arrest and display profound changes in nuclear and chromatin organization, gene expression, cell metabolism and secretory profile[2]. Depending on the physiological context, senescence can be either beneficial or detrimental. Induction of senescence can restrain tumor progression[3] and limit fibrosis[4]; however, the aberrant accumulation of senescent cells contributes to aging and age-related pathologies[5]. Moreover, there is now strong evidence that the selective elimination of senescent cells delays the onset of age-related diseases or at least ameliorates their symptoms[6]. Given the causative role of senescence in the aging process and its contribution to multiple age-related diseases, senescent cells are prime targets for drug-induced elimination (senolysis)[7], but alternative strategies are also pursued. One such strategy is rejuvenating senescent cells[8,9].

The two defining hallmarks of senescent cells are a stable cell-cycle arrest (mediated by the transcriptional upregulation of cyclin-dependent kinase inhibitors such as $p16^{INK4a}$) and the secretion of a complex combination of factors, collectively referred to as the senescence-associated secretory phenotype (SASP). The SASP is widely believed to mediate many of the detrimental effects exerted by senescent cells and consequently, strategies have been devised to target it[10,11]. A progressive induction of senescence, especially in adult stem cell populations has been associated with age-dependent declines in tissue function[12,13]. With age, stem cell populations undergo senescence and, as a result, the ability of the tissue to repair after damage gradually diminishes[14]. Consequently, strategies aimed at alleviating stem cell senescence have the potential to preserve the regenerative potential in aged tissues. As cellular senescence is one of the main impasses for the expansion of stem cells ex vivo, drugs that prevent the onset of senescence could also be used to optimize the generation of stem cells for subsequent cellular therapies.

We have previously performed high-throughput drug screens to identify cardiac glycosides as broad-spectrum senolytics[15]. Here, we followed a similar approach to identify drugs alleviating senescence. We found that treatment with 3DA, an *S*-adenosyl homocysteinase (AHCY) inhibitor[16,17], partially prevents both replicative and oncogene-induced senescence. We confirmed the potential benefits of 3DA treatment in ex vivo cultures and engraftment experiments of

[1]MRC London Institute of Medical Sciences (LMS), London, UK. [2]Institute of Clinical Sciences (ICS), Faculty of Medicine, Imperial College London, London, UK. [3]Centre for Haematology, Department of Immunology and Inflammation, Faculty of Medicine, Imperial College London, London, UK. [4]Department of Cell Biology and Infection, Institut Pasteur, Paris, France. [5]INSERM, U993, Paris, France. [6]IRCM, Institut de Recherche en Cancérologie de Montpellier, INSERM U1194, Université de Montpellier, Institut Régional du Cancer de Montpellier, Montpellier, France. [7]European Research Institute for the Biology of Ageing, University Medical Center Groningen, University of Groningen, Groningen, The Netherlands. [8]Department of Medicine, Hematology and Oncology, Faculty of Medicine, Medical Center University of Freiburg, Freiburg, Germany. [9]Department of Experimental and Health Sciences, Pompeu Fabra University (UPF), CIBER on Neurodegenerative diseases (CIBERNED), Barcelona, Spain. [10]Université de Paris, Sorbonne Paris Cité, Paris, France. [11]Laboratory of In Vivo Genetics & Gene Therapy, Genome Institute of Singapore, Singapore, Singapore. [12]National Cancer Centre, Singapore, Singapore. [13]School of Biological Sciences, Nanyang Technological University, Singapore, Singapore. [14]ICREA, Barcelona, Spain. [15]Spanish National Center on Cardiovascular Research (CNIC), Madrid, Spain. [16]Sanquin Research, and Landsteiner Laboratory, Amsterdam University Medical Center, University of Amsterdam, Amsterdam, The Netherlands. [17]INSERM U955, Université Paris-Est Créteil (UPEC), FHU SENEC, Créteil, France.
✉e-mail: jesus.gil@imperial.ac.uk

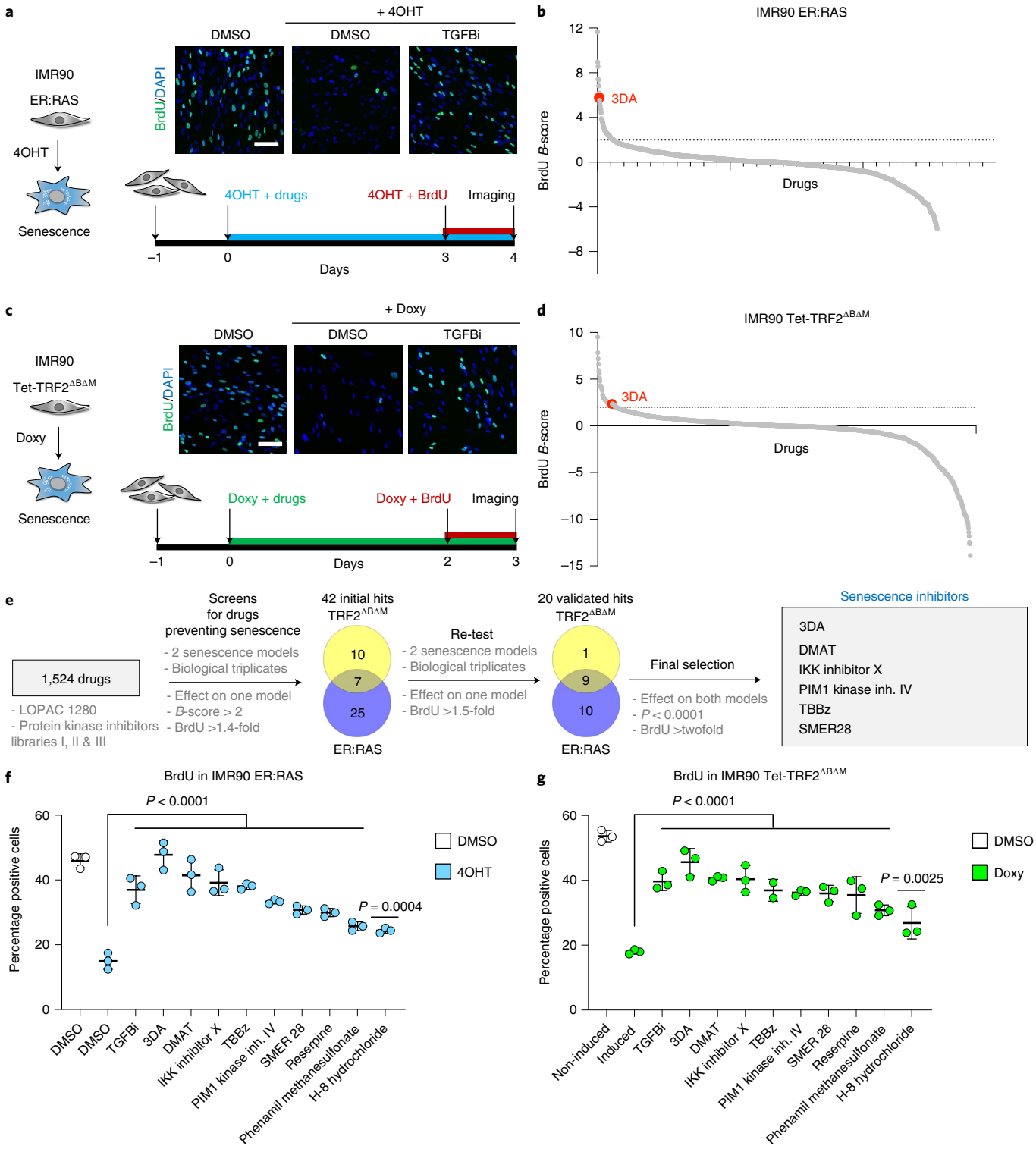

geriatric muscle stem cells and human umbilical cord blood (UCB) cells suggesting that, by inhibiting senescence, 3DA could improve the efficiency of cellular therapies.

Results

Drug screens for compounds alleviating senescence. Senescence can be triggered by multiple stresses, ranging from oncogenic activation to replicative exhaustion or treatment with chemotherapeutic drugs[1]. To identify compounds that prevent or alleviate senescence, we used two different models of cellular senescence. First, we took advantage of a widely used model of oncogene-induced senescence (OIS)[18], in which a 4-hydroxytamoxifen (4OHT)-inducible oncogenic RAS chimeric protein ER:RAS^{V12} is expressed in IMR90 human fibroblasts (Extended Data Fig. 1a). We also used a second model in which the expression of a dominant-negative, doxycycline-inducible TRF2 protein, TRF2$^{\Delta B\Delta}$ (refs. [19,20]) induces telomere dysfunction to cause senescence (Extended Data Fig. 1b–f). As a positive control for preventing senescence induction, we treated

Fig. 1 | Screen for drugs alleviating senescence identifies 3DA. a, Screen in a model of OIS. Representative immunofluorescence images (top). BrdU incorporation, which indicates proliferation, is shown in green. TGFBi is included as a positive control. Scale bar, 100 µm. Experimental design for the screen in OIS using inducible IMR90 ER:RAS cells (bottom). DAPI, 4,6-diamidino-2-phenylindole. **b**, BrdU raw values for the screen were normalized using the *B*-score method. 3DA is highlighted in red. **c**, Screen in a model of senescence induced by telomere uncapping. Representative immunofluorescence images (top). BrdU incorporation, which indicates proliferation, is shown in green. Scale bar, 100 µm. Experimental design for the screen in IMR90 tet-TRF2$^{\triangle B\triangle M}$ cells (bottom). Doxy, doxycycline. **d**, BrdU raw values for the screen were normalized using the *B*-score method. 3DA is highlighted in red. **e**, Summary of the screens for drugs alleviating senescence. Venn diagrams (not to scale) show number of drugs passing the filters and overlap between replicative and OIS. DMAT, 2-dimethylamino-4,5,6,7-tetrabromo-1H-benzimidazole; TBBz, 4,5,6,7-tetrabromobenzimidazole; IKK, IkappaB kinase; PIM1, proviral integration site for Moloney murine leukemia virus 1; SMER28, 6-bromo-N-2-propenyl-4-quinazolinamine. **f**, Quantification of immunofluorescence staining for BrdU of IMR90 ER:RAS cells 4 d after treatment with 4OHT or vehicle (DMSO) and the nine senescence inhibitors validated in the screen in both senescence models ($n=3$). **g**, Quantification of immunofluorescence staining for BrdU of IMR90 tet-TRF2$^{\triangle B\triangle M}$ cells 3 d after treatment with doxycycline or vehicle (DMSO) and the nine senescence inhibitors validated in the screen in both senescence models ($n=3$). All statistical significances were calculated using one-way analysis of variance (ANOVA). All error bars represent mean ± s.d; *n* represents independent experiments.

cells undergoing senescence with 4 µM transforming growth factor (TGF)-β RI kinase inhibitor II (TGFBi), which resulted in a higher percentage of cells incorporating 5-bromodeoxyuridine (BrdU) when compared to untreated cells[18] (Fig. 1a,c). We assessed the effect that 1,524 drugs (part of the LOPAC 1280 and the Inhibitor-Select Protein kinase inhibitor libraries I, II and III) have on cells undergoing OIS and after normalization, selected 32 initial hits for further testing (*B*-score >2 and BrdU 1.4-fold higher than the control; Fig. 1b).

To identify drugs that behave as general inhibitors of senescence, we screened the same library on cells expressing TRF2$^{\Delta B\Delta M}$ and selected 17 hits that delayed senescence arrest (Fig. 1d). Seven of these drugs have also been identified in the screen on IMR90 ER:RAS cells. We took forward 42 drugs selected from both screens (Fig. 1e). Re-testing in both models of senescence validated 20 drugs that partially prevented the senescence growth arrest in at least one of the models. Nine out of these 20 drugs have an effect in both senescence models (Fig. 1f–g). By imposing more strict criteria ($P<0.0001$ and BrdU more than twofold higher than the control), we identified six compounds (Fig. 1e, right) with the ability to alleviate senescence (Fig. 1e). Among those, 3DA, an AHCY inhibitor[16,17] performed consistently well in both systems and was selected as a candidate drug to alleviate senescence.

Treatment with 3DA alleviates senescence. To investigate the ability of 3DA to alleviate senescence, we used the IMR90 Tet-TRF2$^{\Delta B\Delta M}$ model. 3DA partially prevented the growth arrest associated with senescence in a dose-dependent manner in this model (Fig. 2a). While expression of TRF2$^{\Delta B\Delta M}$ causes telomere uncapping and results in a DNA damage response that mimics what we observed during senescence[21], we decided to assess the effect that treatment with 3DA has on cells undergoing replicative senescence. We therefore treated IMR90 fibroblasts with 3DA. We observed a gradual loss of replicative potential in IMR90 cells during serial passage as measured by assessing the percentage of cells incorporating BrdU (Fig. 2b, middle). Concurrently, treatment with 3DA increased the subset of cells dividing at each passage, resulting in an extension of the replicative potential of old cells (Fig. 2b, middle and right).

To further assess the ability of 3DA to alleviate senescence, we used IMR90 ER:RAS. Treatment with 3DA prevented the growth arrest associated with OIS in a dose-dependent manner as assessed by BrdU incorporation (Fig. 2c, middle) and colony formation (Fig. 2c, right). The effect that 3DA had on alleviating senescence was further confirmed as the induction of SA-β-galactosidase activity was impaired in 3DA-treated cells (Fig. 2d). Demonstrating the global effect caused by 3DA on senescence induction, treatment with 3DA partially prevented the upregulation of p16^{INK4a} (Fig. 2e and Extended Data Fig. 2a,b) and p21^{CIP1} (Extended Data Fig. 2c). While the above results provide evidence that 3DA treatment facilitates senescence bypass, 3DA does not promote senescence escape (Extended Data Fig. 2d). Notably, treatment with 3DA for 2 weeks (followed by 2 weeks off 3DA) still results in a higher percentage of proliferating cells and lower levels of p16^{INK4a} when compared to control (dimethylsulfoxide (DMSO)-treated) cells (Extended Data Fig. 2e). This experiment suggests that a transient treatment with 3DA alleviates senescence and produces beneficial effects extending beyond the treatment time.

AHCY knockdown prevents induction of senescence. 3DA inhibits AHCY[16]. To understand whether prevention of senescence by 3DA is due to on-target inhibition of AHCY, we designed two short hairpin RNA (shRNA) vectors that knocked down AHCY (Extended Data Fig. 3a). AHCY depletion increased the proliferative potential of old IMR90 cells, as assessed by colony formation (Fig. 3a, middle) and BrdU incorporation (Fig. 3a, right). Moreover, knockdown of AHCY resulted in reduced senescence of IMR90 cells, as shown by a decrease in the percentage of cells positive for SA-β-galactosidase (Fig. 3b), p16^{INK4a} expression (Fig. 3c) and DNA damage (Extended

Fig. 2 | Treatment with 3DA attenuates replicative and oncogene-induced senescence. a, Quantification of immunofluorescence staining for BrdU of IMR90 tet-TRF2$^{\triangle B\triangle M}$ cells 3 d after treatment with doxycycline or vehicle (DMSO) and increasing concentrations of 3DA ($n=4$) (left). The statistical significance was calculated using one-way ANOVA. Representative immunofluorescence images (right). BrdU incorporation, which indicates proliferation, is indicated in red. Scale bar, 100 µm. **b**, Quantification of immunofluorescence staining for BrdU in young (population doubling (PD) 24) versus old (PD ~38–44) IMR90 cells after treatment with 10 µM 3DA or vehicle (DMSO) ($n=3$) (left). The statistical significance was calculated using unpaired two-tailed Student's *t*-tests. Crystal violet-stained, young and old IMR90 cells treated with 3DA or vehicle (DMSO) (right). Images are a representative experiment out of three. **c**, Quantification of immunofluorescence staining for BrdU of IMR90 ER:RAS cells 4 d after treatment with 4OHT or vehicle (DMSO) and increasing concentrations of 3DA ($n=4$) (left). The statistical significance was calculated using one-way ANOVA. Right, crystal violet-stained, six-well dishes of IMR90 ER:RAS cells treated with 3DA or vehicle (DMSO). Images are a representative experiment out of three. **d**, Representative images of SA-β-galactosidase staining of IMR90 ER:RAS cells 8 d after treatment with 4OHT or vehicle (DMSO) and 3DA (left); quantification ($n=3$) (right). Statistical significance was calculated using a one-way ANOVA. Scale bar, 100 µm. **e**, Single-cell nuclear intensity values for p16^{INK4a} in control and senescent IMR90 ER:RAS cells treated with 10 µM 3DA or vehicle (DMSO) for 6 d in a representative experiment out of 4 ($n=200$ cells per condition). The statistical significance was calculated using unpaired two-tailed Student's *t*-test. All error bars represent mean ± s.d; *n* represents independent experiments.

Data Fig. 3b). Two other AHCY inhibitors, 3-deazaneplanocin (DZNep) and D-eritadenine (D-Erit), also prevented the growth arrest associated with OIS induction, further suggesting that the effect is on-target (Extended Data Fig. 3c). Knockdown of AHCY (Extended Data Fig. 3d) also prevented OIS, alleviating the senescent cell growth arrest (Fig. 3d), resulting in a decreased percentage of cells positive for SA-β-galactosidase (Fig. 3e) and reduced expression of $p16^{INK4a}$ (Extended Data Fig. 3e). Of note, *AHCY* expression was upregulated in cells undergoing OIS (Extended Data Fig. 3d). To better understand how AHCY knockdown impacts senescence

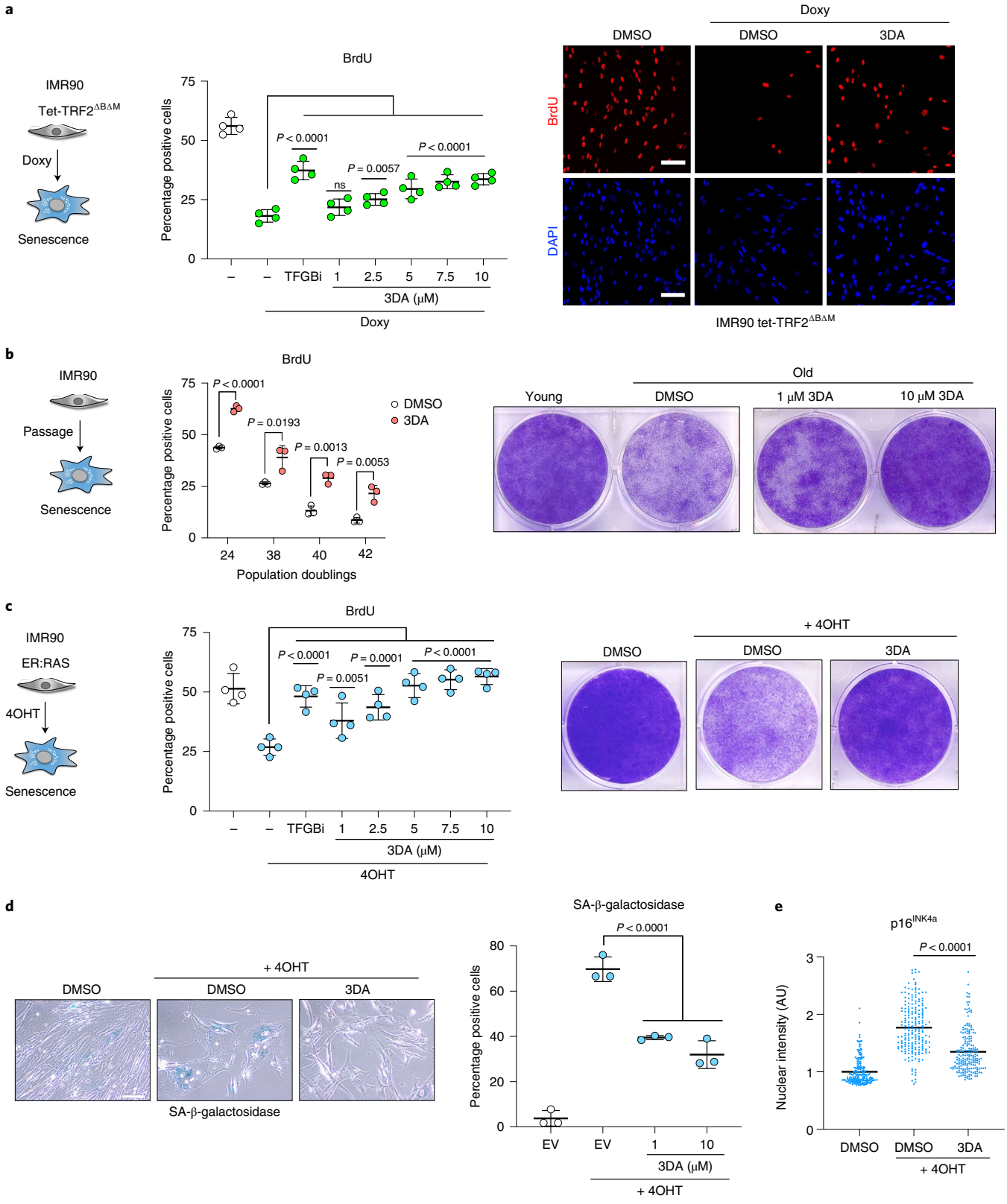

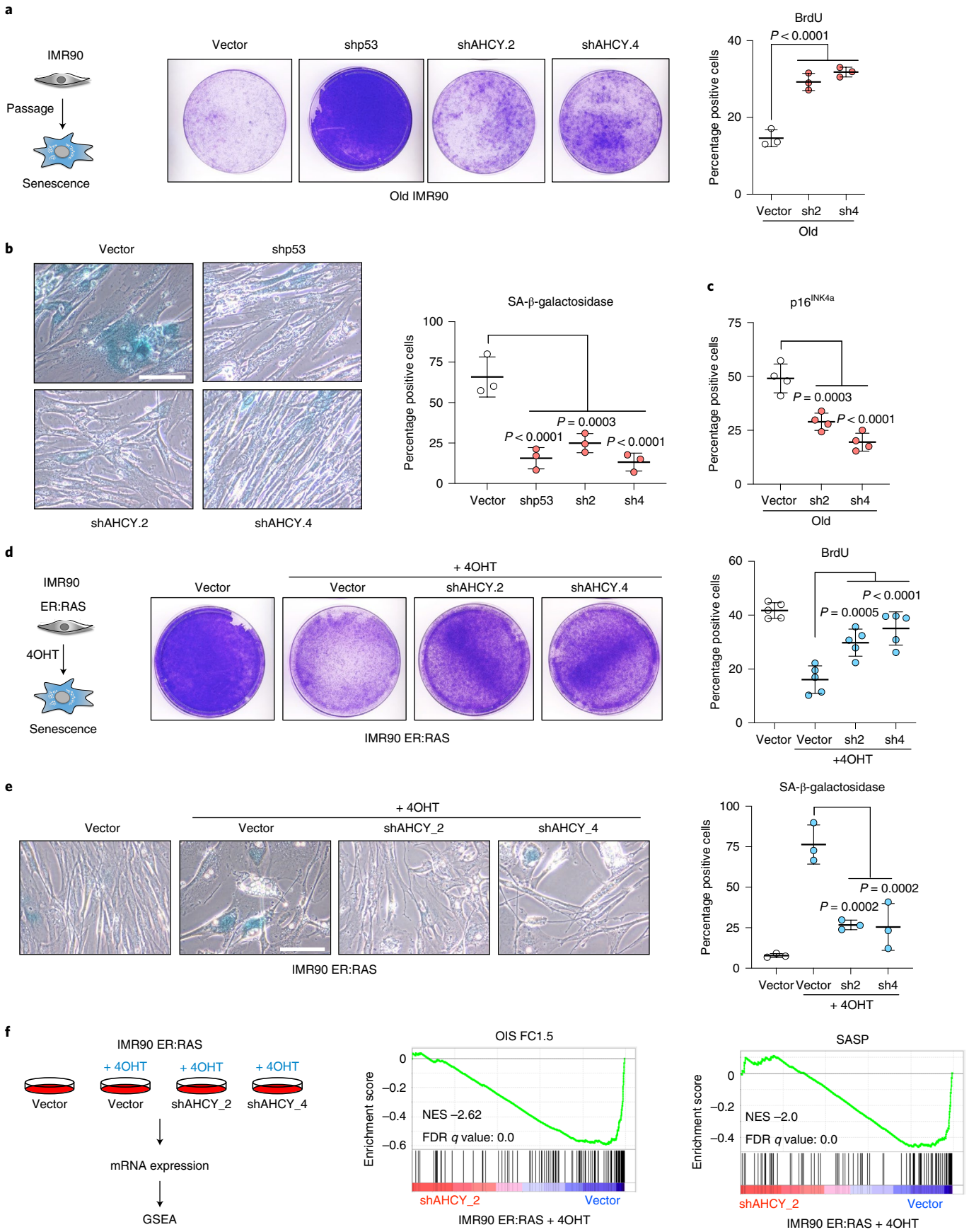
a
IMR90
Passage
Senescence
Vector
shp53
shAHCY.2
shAHCY.4
Old IMR90
BrdU
P < 0.0001
Percentage positive cells
Vector
sh2
sh4
Old
b
Vector
shp53
shAHCY.2
shAHCY.4
SA-β-galactosidase
P = 0.0003
P < 0.0001
P < 0.0001
Vector
shp53
sh2
sh4
c
p16INK4a
P = 0.0003
P < 0.0001
Old
d
IMR90
ER:RAS
4OHT
Senescence
+ 4OHT
IMR90 ER:RAS
BrdU
P < 0.0001
P = 0.0005
+4OHT
e
shAHCY_2
shAHCY_4
SA-β-galactosidase
P = 0.0002
P = 0.0002
f
IMR90 ER:RAS
mRNA expression
GSEA
OIS FC1.5
Enrichment score
NES –2.62
FDR q value: 0.0
IMR90 ER:RAS + 4OHT
SASP
NES –2.0
FDR q value: 0.0

Fig. 3 | *AHCY* knockdown attenuates OIS and replicative senescence. a, Crystal violet-stained, old (PD ~40–44) IMR90 cells infected with different pGIPZ shRNAs against *AHCY*, *TP53* or the parental pGIPZ vector (left). Images are from a representative experiment out of three. Quantification of immunofluorescence staining for BrdU incorporation in cells from the same experiment ($n=3$) (right). **b**, Representative images of SA-β-galactosidase staining (left). Scale bar, 100 μm; quantification ($n=3$) (right). **c**, Quantification of cells expressing $p16^{INK4a}$ as measured by immunofluorescence (IF) ($n=4$). **d**, Crystal violet-stained, cultures of IMR90 ER:RAS cells infected with different pGIPZ shRNAs against *AHCY*, *TP53* or the parental pGIPZ vector (left). Images are a representative experiment out of three. Quantification of IF staining for BrdU of cells from the same experiment ($n=5$) (right). **e**, Representative images of SA-β-galactosidase staining. Scale bar, 100 μm (left); quantification ($n=3$) (right). **f**, Experimental design for transcriptional profiling of IMR90 ER:RAS cells infected with two different pGIPZ shRNAs against *AHCY* or the parental pGIPZ vector (left). GSEA signatures for OIS and SASP (right). NES, normalized enrichment score; FDR, false discovery rate. All statistical significances were calculated using one-way ANOVA. All error bars represent mean ± s.d; *n* represents independent experiments.

onset, we performed transcriptome analysis of senescent cells after AHCY knockdown (Fig. 3f and Extended Data Fig. 3f–h). Principal-component analysis (PCA) placed cells with reduced AHCY expression in an intermediate position between growing and senescent cells (Extended Data Fig. 3f). Gene set enrichment analysis (GSEA) further confirmed that depletion of AHCY with two independent shRNAs prevented senescence and caused downregulation of the SASP while increasing proliferation (Fig. 3f and Extended Data Fig. 3g,h). Overall, the above results indicate that inhibition or depletion of AHCY prevents senescence onset.

Impaired histone H3K36 methylation upon 3DA treatment. 3DA inhibits AHCY, leading to the accumulation of adenosyl-homocysteine and to by-product inhibition of *S*-adenosyl-L-methionine (SAM)-dependent methyltransferases[22]. Notably, AHCY inhibition has been shown to affect the activity of a specific histone methylase, EZH2 (that methylases H3K27) in cancer cells[23]; however, treatment with either GSK126 (an inhibitor of the H3K27 methylase EZH2), BRD4770 (an inhibitor of the H3 K9 methylase EHMT2) or EPZ004777 (an inhibitor of the H3 K79 methylase DOT1L) exacerbated, rather than prevented, senescence (Extended Data Fig. 4a). To investigate whether 3DA affects histone methylation, we analyzed different histone marks by western blot. H3K36me3 was the only histone mark reduced in 3DA-treated senescent cells (Fig. 4a). Consistent with the overall decrease of H3K36me3 levels, we detected a higher H3K36me1 level in 3DA-treated senescent cells (Extended Data Fig. 4b). Taking advantage of quantitative immunofluorescence, we observed that treating cells undergoing OIS with 3DA resulted in lower levels of H3K36me3. The latter was quantified at the single-cell level using a stringent threshold (Fig. 4b and Extended Data Fig. 4c). This difference was not linked to a change in overall histone 3 levels (Extended Data Fig. 4d), was already present at the early stages of OIS induction (Fig. 4b; day 4) and persisted upon senescence establishment (Extended Data Fig. 4e; day 6).

To dissect further the gene-regulatory mechanism of 3DA treatment, we determined global gene expression profiles by RNA-seq. We comprehensively mapped genomic H3K36me3 by ChIP-seq in proliferating (DMSO), senescent (4OHT plus DMSO) and 3DA-treated senescent cells (4OHT plus 3DA; Fig. 4c). Transcriptome PCA analysis, showed that senescent cells treated with 3DA, clustered with senescent cells in which AHCY has been knocked down and were found in an intermediate place between growing and senescent cells (Extended Data Fig. 5a,b). GSEA confirmed that 3DA treatment prevented senescence, resulting in downregulation of the SASP and other senescence signatures and upregulation of E2F-related signatures (Extended Data Fig. 5c,d). Methylation of H3K36 is mostly associated with transcription of active euchromatin, although it has also been implicated in other processes[24]. Notably, GSEA showed an enrichment of H3K36me3 levels in SASP genes during OIS (Extended Data Fig. 5e). Integrative analysis revealed a genome-wide positive correlation ($R=0.51$, $P<10^{-16}$; Fig. 4d) between H3K36me3 levels and transcriptome changes in senescent cells when compared to proliferating cells. The correlation was weaker when senescent cells were compared to 3DA-treated senescent cells ($R=0.20$, $P<10^{-16}$; Fig. 4e). The data suggested that 3DA impacts H3K36me3 levels and transcription differentially across the genome. To stratify and visualize this differential impact, we performed *k*-means clustering and functional over-representation profiling (Fig. 4f), which identified five correlated H3K36me3 gene expression modules (Supplementary Table 1), revealing three key features. First, H3K36me3 levels drop globally upon 3DA treatment in senescent cells (664 among a total of 1,926 regions; modules 2 and 3; Fig. 4f), thus, corroborating the immunoblot results of Fig. 4a and this drop is mirrored, mostly, in a decrease in gene expression (3DA-responsive genes). Second, some loci notably accumulate (268 among a total of 1,926 regions; cluster 4) or display no change in H3K36me3 levels (994 among a total of 1,926 regions, modules 1 and 5) (3DA-unresponsive genes) and this is mirrored in an increase or no change in gene expression. Third, functional over-representation profiles disclosed that among the 3DA-responsive genes (modules 2 and 3) (genes that showed a concomitant decrease in H3K36me3 levels and gene expression), there was a subset of SASP genes such

Fig. 4 | 3DA treatment affects histone H3K36 methylation during OIS. a, Immunoblots of histones extracted from IMR90 ER:RAS cells after 4OHT induction and treatment with 10 μM 3DA or vehicle (DMSO). Immunoblot of histone H3 is included as a sample processing control. Immunoblots are a representative experiment out of three. **b**, Representative immunofluorescence images of H3K36me3 staining (red) in IMR90 ER:RAS cells 4 d after 4OHT induction (left). Cells were treated with 10 μM 3DA or vehicle (DMSO). Scale bar, 100 μm; quantification ($n=5$) (right). Statistical significances were calculated using one-way ANOVA. Error bars represent mean ± s.d; *n* represents independent experiments. **c**, Experimental design for transcriptional profiling of IMR90 ER:RAS cells 6 d after after 4OHT induction and treatment with 10 μM 3DA or vehicle (DMSO). **d**, Fold–fold plot comparing fold change in gene expression and ChIP-seq signal in 4OHT versus DMSO treatment. **e**, Fold–fold plot comparing fold change in gene expression and ChIP-seq signal in 3DA versus 4OHT treatment. The Pearson's product-moment correlation *R* and the associated *P* value are reported in **d** and **e**. **f**, Heat map depicting the level of H3K36me3 ChIP-seq signal (*z* score) and the expression level of the closest/overlapping genes (*z* score) for peaks defined as differential between DMSO + OHT versus DMSO or 3DA + OHT versus DMSO. ChIP-seq data were partitioned into five modules using *k*-means clustering. Example genes are displayed on the right side for each module. **g**, Functional over-representation map depicting enriched hallmark genesets for each module. Circles are color coded according to the FDR-corrected *P* values based on the hypergeometric test. Size is proportional to the percentage of genes in the hallmark gene set belonging to the cluster. **h**,**i**, Representative genome browser snapshots showing H3K36me3 normalized signal at *IL1B* (module 2, **h**) and *CDK1* (module 4, **i**) gene loci for DMSO (orange), DMSO + 4OHT (green) and 3DA + 4OHT (violet) conditions. Data are expressed as normalized counts per million reads in 200-bp non-overlapping windows.

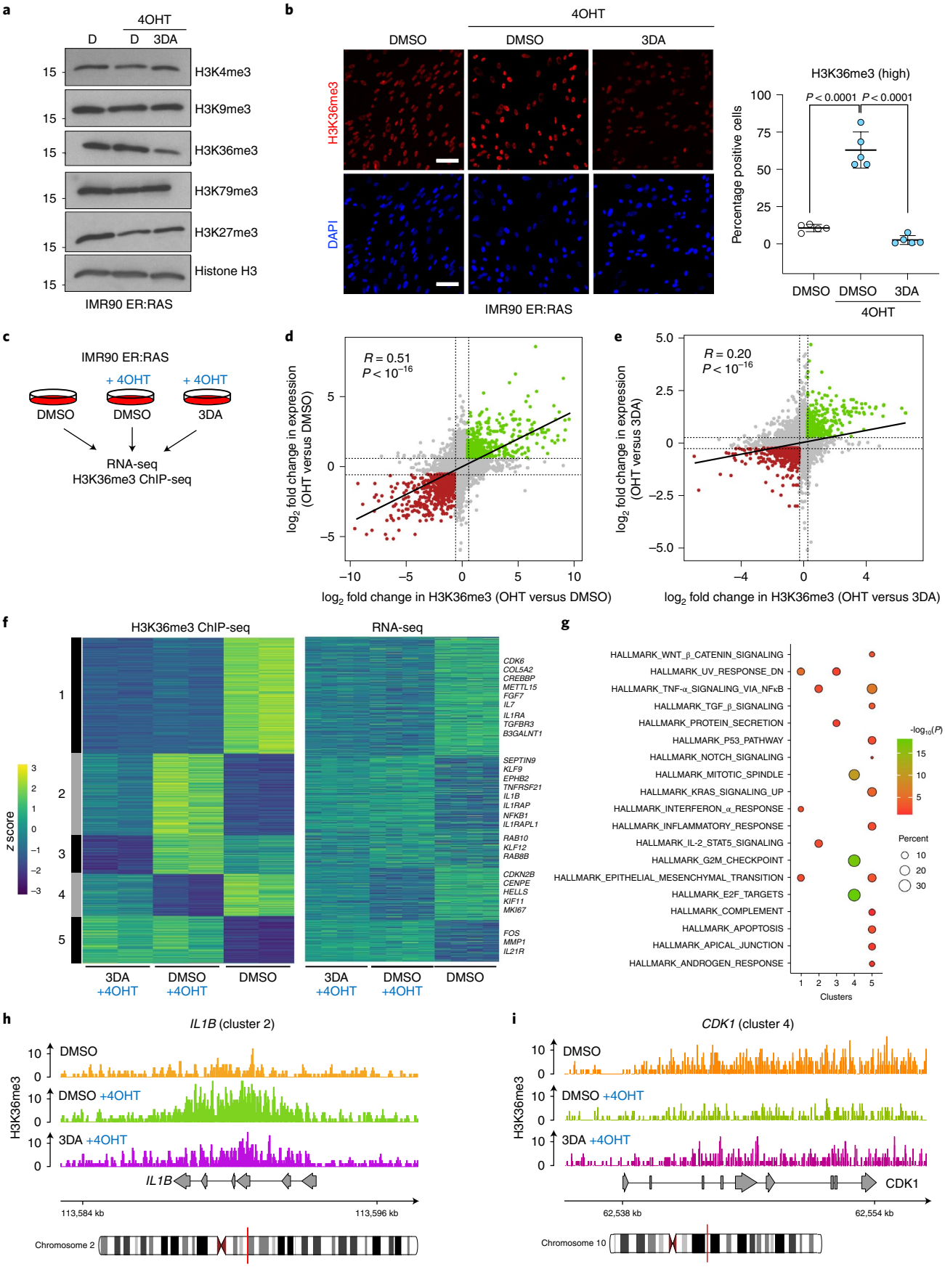
a
4OHT
D
D
3DA
15
H3K4me3
H3K9me3
H3K36me3
H3K79me3
H3K27me3
Histone H3
IMR90 ER:RAS
b
4OHT
DMSO
DMSO
3DA
H3K36me3
DAPI
IMR90 ER:RAS
H3K36me3 (high)
P < 0.0001
P < 0.0001
Percentage positive cells
DMSO
DMSO
3DA
4OHT
c
IMR90 ER:RAS
+ 4OHT
+ 4OHT
DMSO
DMSO
3DA
RNA-seq
H3K36me3 ChIP-seq
d
R = 0.51
P < 10−16
log2 fold change in expression (OHT versus DMSO)
log2 fold change in H3K36me3 (OHT versus DMSO)
e
R = 0.20
P < 10−16
log2 fold change in expression (OHT versus 3DA)
log2 fold change in H3K36me3 (OHT versus 3DA)
f
H3K36me3 ChIP-seq
RNA-seq
z score
CDK6
COL5A2
CREBBP
METTL15
FGF7
IL7
IL1RA
TGFBR3
B3GALNT1
SEPTIN9
KLF9
EPHB2
TNFRSF21
IL1B
IL1RAP
NFKB1
IL1RAPL1
RAB10
KLF12
RAB8B
CDKN2B
CENPE
HELLS
KIF11
MKI67
FOS
MMP1
IL21R
3DA +4OHT
DMSO +4OHT
DMSO
g
HALLMARK_WNT_β_CATENIN_SIGNALING
HALLMARK_UV_RESPONSE_DN
HALLMARK_TNF-α_SIGNALING_VIA_NFκB
HALLMARK_TGF_β_SIGNALING
HALLMARK_PROTEIN_SECRETION
HALLMARK_P53_PATHWAY
HALLMARK_NOTCH_SIGNALING
HALLMARK_MITOTIC_SPINDLE
HALLMARK_KRAS_SIGNALING_UP
HALLMARK_INTERFERON_α_RESPONSE
HALLMARK_INFLAMMATORY_RESPONSE
HALLMARK_IL-2_STAT5_SIGNALING
HALLMARK_G2M_CHECKPOINT
HALLMARK_EPITHELIAL_MESENCHYMAL_TRANSITION
HALLMARK_E2F_TARGETS
HALLMARK_COMPLEMENT
HALLMARK_APOPTOSIS
HALLMARK_APICAL_JUNCTION
HALLMARK_ANDROGEN_RESPONSE
-log10(P)
Percent
Clusters
h
IL1B (cluster 2)
H3K36me3
DMSO
DMSO +4OHT
3DA +4OHT
IL1B
113,584 kb
113,596 kb
Chromosome 2
i
CDK1 (cluster 4)
H3K36me3
DMSO
DMSO +4OHT
3DA +4OHT
CDK1
62,538 kb
62,554 kb
Chromosome 10

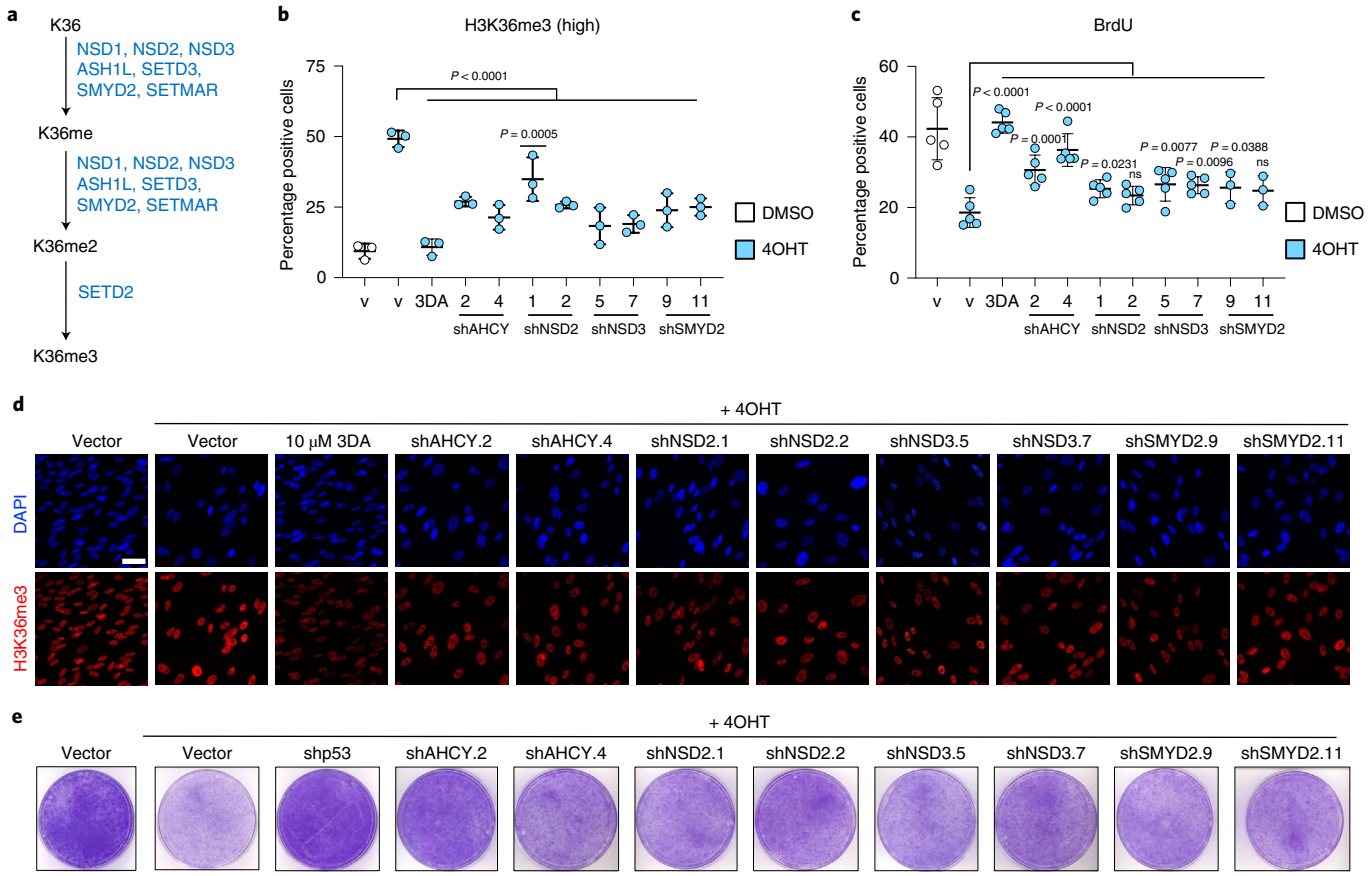

Fig. 5 | Interfering with H3K36 methyltransferases affects senescence induction. a, Eight different methyltransferases: NSD1, NSD2, NSD3, ASH1L, SETD2, SETD3, SMYD2 and SETMAR are involved in the sequence leading to histone H3 trimethylation at lysine 36. **b**, Quantification of immunofluorescence staining for H3K36me3 7 d after vehicle (DMSO) or 4OHT induction of IMR90 ER:RAS cells infected with different pGIPZ shRNAs against NSD2, NSD3, SMYD2, AHCY or the parental pGIPZ vector ($n = 3$). Treatment with 3DA was included as positive control. **c**, Quantification of immunofluorescence staining for BrdU 4 d after vehicle (DMSO) or 4OHT induction from the experiment described in **b** ($n = 5$ except for SMYD2 $n = 3$). **d**, Representative immunofluorescence images of H3K36me3 staining (red). Scale bar, 50 μm. Quantification is shown in **b**. **e**, Crystal violet-stained, 10-cm dishes of IMR90 ER:RAS from the experiment described in **b**. All statistical significances were calculated using one-way ANOVA. All error bars represent mean ± s.d; *n* represents independent experiments.

as *IL1B* (Fig. 4g,h) and *IL12RB2* (Extended Data Fig. 5f). Of note, among the genes showing an increase in H3K36me3 levels and gene expression (module 4), were many E2F targets involved in cell cycle progression, such as *CDK1* (Fig. 4i) or *CENPF* (Extended Data Fig. 5g). Together, our data suggest that 3DA treatment differentially impacts H3K36me3 to affect senescence.

Disrupting H3K36 methylation affects senescence induction. The changes in H3K36 methylation might explain how 3DA prevents senescence or could just be a consequence of senescence prevention. To distinguish between these two possibilities, we decided to target H3K36 methylation directly. Given that at least eight methyltransferases regulate H3K36 methylation (Fig. 5a), we decided to test how three of these enzymes (NSD2, NSD3 and SMYD2) affect H3K36me3 and growth arrest during OIS. To this end, we generated shRNAs targeting NSD2, NSD3 and SMYD2 (Extended Data Fig. 6a–c). Knockdown of these methyltransferases resulted in reduced overall H3K36me3 levels during OIS (Fig. 5b,d and Extended Data Fig. 6d). Knockdown of these enzymes partially prevented the growth arrest induced during OIS, as assessed measuring BrdU incorporation (Fig. 5c) or assessing colony formation (Fig. 5e). The extent of prevention achieved upon knockdown of NSD2, NSD3 or SMYD2 was lower than that caused by knockdown of AHCY or treatment with 3DA, suggesting redundancy and opening the possibility to other additional mechanisms. Overall, our results indicate that 3DA prevents senescence, at least in part, through indirect inhibition of H3K36 methyltransferases.

3DA enhances engraftment of geriatric muscle stem cells. The accumulation of senescent cells contributes to aging and disease and limits the proliferative potential of old cells, including stem cells[5]. Notably, the AHCY inhibitor DZNep has been shown to facilitate the generation of induced pluripotent stem cells (iPSCs) by stimulating Oct4 expression[25]. We previously showed that senescence limits the generation of iPSCs, a process termed reprogramming-induced senescence (RIS)[26]. Therefore, we asked the question as to whether 3DA could also inhibit RIS. IMR90 fibroblasts were transduced with a retroviral vector expressing reprogramming factors (OCT4, SOX2, KLF4 and cMYC, collectively referred to as OSKM; Extended Data Fig. 7a). Indeed, treatment with 1 μM 3DA prevented the senescence-associated growth arrest induced during reprogramming (Extended Data Fig. 7b).

To investigate whether 3DA can mitigate the detrimental effects of physiological age-induced senescence, we used skeletal muscle stem cells (also known as satellite cells) from very old (geriatric) mice. Satellite cells sustain skeletal muscle regeneration and their regenerative decline at geriatric age has been attributed to senescence entry and loss of proliferative potential[14]. Of note, induction

of autophagy by rapamycin treatment can prevent senescence and induce proliferation in cultured geriatric satellite cells[27]. Accordingly, we next tested the functional consequences of 3DA treatment on satellite cells isolated from geriatric mice, using rapamycin as an experimental control (Fig. 6a). We observed that treatment with 3DA reduced the percentage of senescent geriatric satellite cells, as assessed by SA-β-galactosidase staining (Fig. 6a) or by quantifying the expression of *Ink4a* (that encodes for $p16^{Ink4a}$; Fig. 6a), *Cdkn1a* (that encodes for $p21^{Cip1}$; Extended Data Fig. 8a) and the intensity of γ-H2A.X (as indicator of DNA damage; Extended Data Fig. 8b,c). Satellite cells derived from young mice were analyzed in parallel as a negative control for senescence entry (Fig. 6a). While treatment of myoblasts with 3DA was described to induce differentiation into myofibers[28], a higher proportion of geriatric satellite cells treated with 3DA or rapamycin retained replicative potential, as measured by quantification of BrdU incorporation (Extended Data Fig. 8d), consistent with reduced expression of myogenic differentiation-specific genes (myogenin, *Myog* and myosin heavy chain 3, *Myh3*) (Extended Data Fig. 8e,f).

To investigate whether 3DA (or rapamycin) treatment could rescue the cell-intrinsic regenerative block of geriatric cells, we engrafted young and geriatric satellite cells (pre-treated with 3DA or rapamycin, or the control vehicle and stained with Dil) into pre-injured muscles of immunodeficient recipient mice (Fig. 6b). We found that 3DA treatment significantly restored expansion of geriatric cells after a 4 d engraftment (Fig. 6b). To assess the functional impact, we treated freshly isolated satellite cells from young and geriatric animals with 3DA or vehicle, labeled with green fluorescent protein (GFP) and injected them into pre-injured immunodeficient mice. Six days after transplantation, we assessed the number and size of the GFP^+ fibers derived from the engrafted satellite cells (Fig. 6c). As expected[29], we observed a marked decrease in the engrafting potential of geriatric satellite cells compared to young cells. Notably, pre-treatment with 3DA restored the engrafting and regenerative capacity of geriatric satellite cells, as observed by the increased number of the newly generated GFP^+ fibers and their larger cross-sectional area (CSA), similar to that obtained by engraftment of young satellite cells (Fig. 6c).

In addition, treatment of mice with 3DA reduced the number of SA-β-$galactosidase^+$ cells in injured muscle (Extended Data Fig. 8g,h). Overall, the above results suggest that the ability of 3DA to prevent senescence is not restricted to fibroblasts but extends to somatic stem cells. Treatment with 3DA alleviates the detrimental effects of senescence, ameliorates the age-associated loss of stem cell function in vivo under tissue regeneration conditions and has functional implications, such as the qualitative and quantitative enhanced formation of myofibers in response to muscle injury.

Preliminary results from a model of liver regeneration in aged mice showed that pre-treatment with 3DA reduces the number of cells showing DNA damage and enhances their regenerative potential after partial liver resection (Extended Data Fig. 9a–c). In addition, histological assessment of the livers from aged mice treated with 3DA showed an improvement in several pathological parameters (Extended Data Fig. 9d–g). An increase in glycogen aggregates had been observed in senescent cells and aged tissues[30]. Treatment with 3DA resulted in reduced diffuse glycogen swelling (Extended Data Fig. 9d). Liver regeneration is normally driven by hepatocyte proliferation. Oval cell hyperplasia is used as an alternative regeneration mechanism when hepatocyte proliferation is impaired (for example when hepatocytes are driven into senescence)[31,32]. Oval cell hyperplasia was present in control mice but was largely absent in mice treated with 3DA (Extended Data Fig. 9f). These experiments further suggest that 3DA can positively impact regeneration by targeting cellular senescence.

3DA ex vivo improves umbilical cord blood cells engraftment. Allogeneic transplantation of hematopoietic stem cells (HSCs) is a standard therapy for many blood disorders. UCB is a source of HSCs for transplant that allows for less stringent cross-matching and results in lower incidence of graft versus host disease[33]. A factor limiting a more widespread adoption of UCB for transplants is the low number of HSCs found per UCB unit that can compromise grafting efficiency in adults[34]. Ex vivo expansion of HSCs is invariably associated with loss of stem cell potential. We assessed whether treatment with 3DA could increase the frequency of human primitive hematopoietic stem and progenitor cells (HSPCs). To this end, we performed in vitro long-term culture-initiating cell (LTC-IC) assays to detect and quantitate primitive human hematopoietic cells. We cultured sorted $CD34^+$ cells in the presence of 10 µM 3DA for 5 weeks and replaced after 5 weeks the medium through methylcellulose for a further 2 weeks. Treatment with 3DA caused a significant increase in the LTC-IC assays, suggesting that 3DA prevents loss of stem cell potential in human cord-blood-derived HSPCs in vitro (Fig. 7a). In line with these results, in vitro suspension culture of cord-blood-derived $CD34^+$ HSPCs in the presence of 10 µM 3DA for 9 d (Fig. 7b) resulted in an increase in the percentage of UCB cells with stem cell potential ($CD34^+CD38^-$; Fig. 7f and Extended Data Fig. 10g), but not in the total number of cells (Extended Data Fig. 10e).

To elucidate whether the enhanced stem cell potential of 3DA-treated cells was related to the 3DA effect on senescence, we carried out RNA-seq of $CD34^+CD38^-$ cells after 9 d of treatment with 3DA or vehicle (DMSO) (Fig. 7b). This analysis showed a reversion of senescence signatures (Fig. 7c and Extended Data Fig. 10d). Of note, and related to the effect that AHCY inhibitors have on stemness[25], we also observed that treatment with 3DA results in the upregulation of stemness (Fig. 7d) and downregulation of differentiation signatures (Extended Data Fig. 10a,b). The above results suggest that the increase in cell fitness caused by 3DA treatment could relate to both its ability to alleviate senescence and affect stemness.

Because human HSC potential is best evaluated with xenotransplantation studies, we transplanted immunocompromised NSG

Fig. 6 | 3DA enhances the proliferative and engraftment potential of geriatric satellite cells in conditions of muscle damage. a, Experimental design. Satellite cells were isolated from muscles of young (2–3 months, $n = 5$) *versus* geriatric (28–31 months, $n = 7$) mice and were cultured for 7 d. Cells were treated with 10 µM 3DA during 6 d or with 100 ng ml^{-1} rapamycin for 2 d as indicated. Results from these experiments are shown in this figure and Extended Data Fig. 8a–d. Quantification of SA-β-galactosidase (SA-β-gal) staining and expression levels for mouse *Ink4a* mRNA (encoding for $p16^{Ink4a}$) are shown. **b**, Experimental design. Equal numbers of satellite cells isolated from young and geriatric mice, previously treated with 3DA, rapamycin or vehicle, were stained with Dil and transplanted into pre-injured muscle of recipient immunodeficient mice for 5 d. Representative images of Dil^+ cells in cryosections of tibialis anterior muscle after 5 d of engraftment (arrows indicate Dil^+ cells) and quantification of Dil^+ cells ($n = 4$ for young; n = 5 for geriatric) are shown. **c**, Experimental design. Equal numbers of satellite cells, freshly isolated from young and geriatric mice, were treated with 3DA or vehicle, transduced with GFP lentivirus and transplanted into the pre-injured muscle of the recipient immunodeficient mice for 6 d. Representative images of GFP^+ fibers in cryosections of tibialis anterior muscle after 6 d of engraftment and quantification of CSA and the number of GFP^+ fibers ($n = 4$ mice per group). Statistical significances were calculated using two-tailed paired Student's *t*-test for geriatric versus geriatric 3DA (Fig. 6b) and two-tailed unpaired Student's *t*-test for the remaining graphs. All error bars represent mean ± s.d; *n* represents number of mice. Scale bars, 20 µm. This figure was partly generated using Servier Medical Art, provided by Servier, licensed under a Creative Commons Attribution 3.0 unported license.

mice with cells that had been exposed to 3DA for 9 d and compared the engraftment of these cells with cells incubated in DMSO at 18–31 weeks after transplant (Fig. 7e). Even though 3DA treatment did not cause an increase of human CD34$^+$CD38$^-$ cells, nor an increase of total CD45$^+$ population in bone marrow (Extended Data Fig. 10f), we did observe a significant increase of human donor-derived CD45$^+$ cells present in peripheral blood of 3DA-treated CD34$^+$ cells (Fig. 7g and Extended Data Fig. 10h). Notably, none of the mice xenotransplanted with 3DA-treated cells developed leukemia and we did not observe evidence of leukemogenic transformation (Extended Data Fig. 10c), suggesting no acute safety concerns, at least in a transient ex vivo setting. Thus, the above experiments indicate that ex vivo treatment with 3DA during the process of UCB expansion before transplant is sufficient to increase the clonogenic

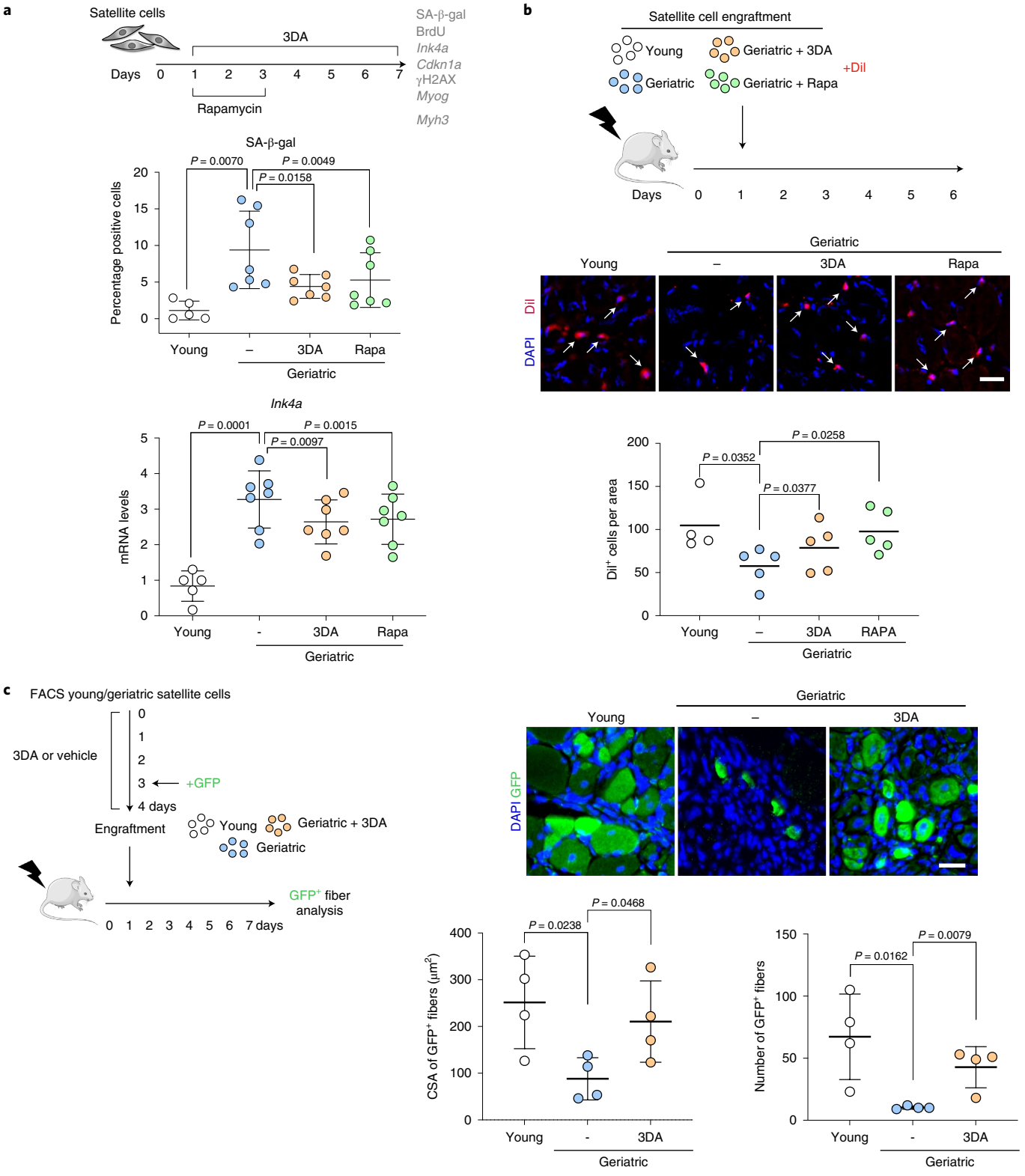

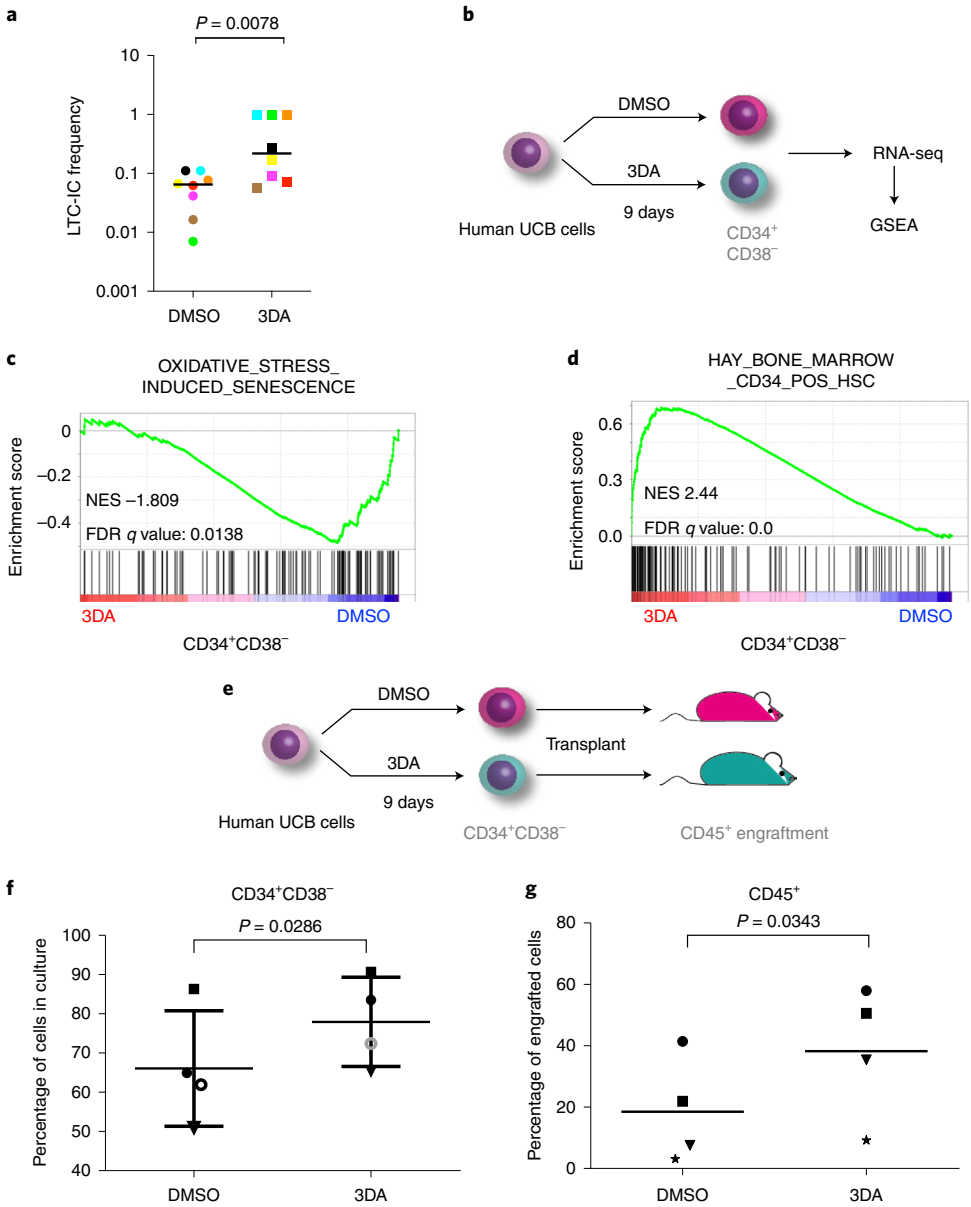

Fig. 7 | 3DA improves the engraftment of UCB cells. a, Frequency of long-term culture-initiating cells of cord-blood-derived CD34+ cells upon treatment with 10 μM 3DA or the vehicle (DMSO). The number of cells that needed to be plated for one LTC-IC to develop is indicated. Identically colored circles/squares indicate paired experimental and control samples that originate from the same cord. Statistical significance was determined using two-tailed Wilcoxon matched-pairs signed-rank test ($n = 8$ independent experiments). **b**, Experimental design for the cord blood RNA-seq experiment. **c**, GSEA signature for oxidative stress-induced senescence. **d**, GSEA signature for Hay bone marrow CD34+ HSCs. **e**, Experimental design for the cord blood transplant experiment. **f**, Cord blood-derived human hematopoietic stem and progenitor (CD34+) cells were treated at day 1, 4 and 7 with 10 μM 3DA or DMSO and analyzed before xenotransplantation at day 9. Changes in cell surface markers CD34 and CD38 were analyzed by flow cytometry. The percentage of CD34+CD38− cells is shown. Data are represented as mean ± s.d. **g**, Cells at 1.5×10^6 from the experiment described in **c** were transplanted into NSG mice. The engraftment of human (CD45+) cells in peripheral blood is significantly higher in the 3DA-treated group. Data are represented as mean. For **f** and **g**, each shape (open circle, closed circle, star, square or triangle) represents a different cord blood sample. Each shape is the average of 2–3 mice transplanted with that cord blood sample ($n = 4$ independent cord blood samples). Statistical significance was determined using two-tailed paired Student's *t*-test.

potential of UCB-derived HSPCs and to preserve their stem cell potential.

Discussion

Research in the last decade has shown how senescent cells accumulate during aging and contribute to pathologies as diverse as cancer, fibrosis and ophthalmological and neurodegenerative disease[5]. Consequently, substantial work has been carried out to target senescence for therapeutic benefit; however, based on genetic evidence for their detrimental role[6,35], most of those efforts have concentrated on finding drugs that selectively kill senescent cells (senolytics)[7] or target the SASP[10,11]. In the present study, we have taken an alternative strategy and screened for drugs that alleviate senescence. Among the compounds identified, 3DA, an AHCY inhibitor, prevented

senescence induced by different stressors. In particular, by using other drugs and shRNAs, we could confirm that the ability of 3DA to alleviate senescence was due to on-target AHCY inhibition.

Inhibition of AHCY leads to adenosyl-homocysteine accumulation and by-product inhibition of SAM-dependent methyltransferases[22]. Notably, the inhibition of AHCY in cancer cells impacted on EZH2-mediated methylation of histone H3K27 (ref. [23]); however, in the context of senescence induction, 3DA does not affect H3K27me3 but rather H3K36me3. H3K36me3 is a mark associated with gene bodies of transcribed genes. Thus, while we observed a global downregulation of H3K36me3 in senescent cells treated with 3DA, H3K36me3 changes were rather gene-specific. Among the genes part of module 2 (showing reduced H3K36me3 and reduced expression on 3DA-treated cells) were SASP components, such as *IL1B* (Fig. 4f–h). As we have previously demonstrated that interfering with interleukin (IL)-1 signaling allows OIS escape[18], this could contribute to explain why treatment with 3DA alleviates senescence. The relation between 3DA, inhibition of H3K36me3 and senescence was confirmed by knockdown of several H3K36 methyltransferases that blunted senescence induction. The partial effects observed might reflect multiple factors, such as the fact that there are at least 8 H3K36me3 methyltransferases and the possibility that 3DA and AHCY affect other undefined pathways impacting on senescence regulation (for example by inhibiting other methyltransferases or through effects mediated by changes in levels of adenosine or homocysteine). Of note, acute NSD2 knockdown can induce senescence[36]. Differences with our study might be caused by the partial NSD2 knockdown that we observe and point to context-dependent effects associated with histone methyltransferase inhibition.

Senescence of adult stem cells causes declines in tissue function[12,13] and this is particularly prominent in old age[14,27]. We have been able to expand the protective role of 3DA to stem cells, including aged stem cells. While injured-induced senescence can facilitate reprogramming in vivo[37], including reprogramming of muscle stem cells (satellite cells)[38], it is well established that adult satellite cells lose their proliferative and regenerative potential during aging due to increased entrance into senescence[14] and our results demonstrate that ex vivo treatment of satellite cells derived from geriatric mice with 3DA rescued these functional defects in vivo by alleviating senescence, resulting in a quantitative and qualitative improved formation of new myofibers derived from geriatric satellite cells in response to muscle injury.

Allogeneic transplantation of UCB is commonly used to treat many blood disorders; however, the efficiency of UCB-based therapies is affected by the low number of available stem cells. Therefore, different strategies have been devised to increase cord blood engraftment. Unbiased screens have identified compounds able to stimulate the expansion ex vivo of human cord blood cells[39,40]. More recently, it has been shown that incubation with the matricellular regulator Nov increases the frequency of serially transplantable HSCs derived from UCB[41]. We reasoned that alleviation of senescence could have similar effects. Therefore, treatment with 3DA could help increase the replicative potential and engrafting ability of UCB cells. Indeed, we observed that treatment with 3DA during the ex vivo expansion phase, increased the clonogenic potential of UCB cells and the number of stem cells present. Consequently, transplantation of these 3DA-treated cells resulted in increased engraftment in peripheral blood. As these effects are achieved after a short ex vivo treatment, this therapy does not present the risks associated with inhibiting senescence in vivo, ranging from negating positive acute senescence responses, to increased cancer risk due to inhibition of OIS. Our analysis did not unveil any evidence of increased oncogenic risk, but this needs to be evaluated more carefully. As 3DA has the potential to cause epigenetic modifications, a long-term safety assessment would be needed before this study can be translated to the clinic. While our results suggest the translational potential of using 3DA to alleviate senescence and promote the efficiency of cell therapies, we have to highlight that this study took advantage of mouse models and further work is needed to establish the potential clinical relevance and feasibility.

In summary, we have identified 3DA as a compound alleviating senescence. 3DA inhibits AHCY and indirectly results in reduced H3K36me3, preventing the expression of components of the senescence program. Thus, our results suggest that 3DA is a candidate drug that could improve the efficiency of cellular therapies, in part, by inhibiting senescence.

Methods

Ethics. This research complied with all relevant ethical regulations and was approved and overseen by five ethics review boards: the ethics committee of the Barcelona Biomedical Research Park (PRBB) and the Catalan Government (Spain) for experiments involving mouse stem cells; the A*STAR Biological Resource Centre (BRC) Institutional Animal Care and Use Committee (IACUC) under protocol no. 191452 (Identification of liver disease intervention points and enhancing liver regeneration) for the mouse liver regeneration experiment; the Medisch Ethisch Toetsings Commissie of Isala Hospital Zwolle (The Netherlands) for the acquisition of human cord blood samples; and the IACUC of the University of Groningen (RUG) under protocol no. AVD1050020209624, for the xenotransplantation studies.

Drugs. The LOPAC 1280 library was acquired from Sigma-Aldrich (LO1280). InhibitorSelect 96-well Protein Kinase Inhibitor Library I (539744), Library II (539745) and Library III (539746) were purchased from Merck. The following compounds were used in this study: doxycycline hydrate (Sigma-Aldrich, D9891), 4OHT (Sigma-Aldrich, H7904), 3DA (Sigma-Aldrich, D8296), InSolution EZH2 inhibitor, DZNep (Merck, 506069), EZSolution GSK126 (BioVision, 2366-1), BRD4770 (Cayman Chemical, 11787), EPZ004777 (Selleckchem S7353), TGFBi (Millipore, 616452) and rapamycin (LC Laboratories).

Antibodies. The following primary antibodies were used in this study: rat monoclonal anti-BrdU (BU1/75(ICR1); Abcam, ab6326) 1:2,000 dilution; mouse monoclonal anti-p16INK4a (JC-8; from CRUK) 1:1,000 dilution; rabbit polyclonal anti-p21 (M-19; Santa Cruz, sc-471) 1:200 dilution; mouse monoclonal anti-SAHH (A-11; Santa Cruz, sc-271389) 1:100 dilution; rabbit anti-phospho-histone H2A.X (Ser139) (Cell Signaling Technology, 2577) 1:50 dilution; mouse monoclonal anti-phospho-histone H2A.X (Ser139) (3F2; Thermo Fisher Scientific, MA1-2022) 1:250 dilution; rabbit polyclonal anti-Ki67 (Abcam, ab15580) 1:200 dilution; rabbit polyclonal anti-53BP1 (Novus Biologicals, NB100-304) 1:1,000 dilution; rabbit monoclonal anti-mono-methyl-histone H3 (Lys36) (D9J1D, Cell Signaling Technology, 14111) 1:1,000 dilution; rabbit monoclonal anti-tri-methyl-histone H3 (Lys36) (D5A7, Cell Signaling Technology, 4909) 1:1,000 dilution; rabbit monoclonal anti-tri-methyl-histone H3 (Lys4) (C42D8; Cell Signaling Technology, 9751) 1:1,000 dilution; rabbit monoclonal anti-tri-methyl-histone H3 (Lys9) (D4W1U; Cell Signaling Technology, 13969) 1:1,000 dilution; rabbit monoclonal anti-tri-methyl-histone H3 (Lys27) (C36B11; Cell Signaling Technology, 9733) 1:1,000 dilution; rabbit polyclonal anti-tri-methyl-histone H3 (Lys79) (Cell Signaling Technology, 4260) 1:1,000 dilution; rabbit polyclonal anti-H3 (Abcam, ab1791) 1:5,000 dilution; and rabbit polyclonal anti-GFP (Invitrogen, A6455) 1:400 dilution. We used the following secondary antibodies: goat anti-mouse IgG (H+L) AlexaFluor594-conjugated (Thermo Fisher Scientific, A11032) 1:500 dilution; goat anti-rat IgG (H+L) AlexaFluor488-conjugated (Thermo Fisher Scientific, A11006) 1:500 dilution; goat anti-rabbit IgG-HRP (Santa Cruz, sc-2004) 1:5,000 dilution; and biotinylated goat anti-rat antibody (Jackson Immunoresearch, 712-066-150) 1:250 dilution.

Cell lines. IMR90 (ATCC CCL-186) cells were obtained from ATCC. IMR90 ER:RAS cells were generated by retroviral infection of IMR90 cells and are described elsewhere[15]. IMR90 tet-TRF2$^{\Delta B\Delta M}$ cells were generated by infecting IMR90 cells with equal amounts of lentivirus-containing rtTA3 and the iCMV-tight vector expressing TRF2$^{\Delta B\Delta M}$ as previously described[20]. IMR90 were cultured in DMEM (Gibco) supplemented with 10% fetal bovine serum (Sigma; tetracycline-free in the case of tet-inducible vectors) and 1% antibiotic-antimycotic solution (Gibco). To induce replicative senescence, IMR90 tet-TRF2$^{\Delta B\Delta M}$ were treated with 50 ng ml^{-1} doxycycline reconstituted in distilled water for 3 d. To induce OIS, IMR90 ER:RAS were treated with 100 nM 4OHT reconstituted in DMSO for 4 d.

Vector construction. pGIPZ-based shRNA targeting *AHCY* (V3LHS_406061, V3LHS_343433), *NSD2* (V3LHS_409073, V3LHS_390121), *NSD3* (V3LHS_354139, V3LHS_343583) and *SMYD2* (V3LHS_381114, V3LHS_381113) were obtained from MRC LMS Genomics core facility. To generate IMR90 ER:RAS-expressing shRNAs, lentiviral infections were carried out as described before[15]. Briefly, HEK293T cells were transfected with the lentiviral and packaging vectors using PEI (PEI 2500, Polysciences). Two days after transfection, HEK293T

viral supernatants were collected, filtered (0.45 µM), diluted 1:4, supplemented with 4 µg ml^{-1} polybrene and added to IMR90 ER:RAS cells plated the day before at a density of 1 million cells per 10-cm dish. Four hours later, lentivirus-containing medium was replaced with fresh medium. Three days after infection, cells were passaged and cultured for 3 d in the presence of 1 µg ml^{-1} puromycin (InvivoGen) to select for infected cells. To generate IMR90 cells expressing reprogramming factors (OSKM), HEK293T cells were transfected with retroviral MSCV-neo vectors expressing a polycistronic cassette encoding Oct4, Sox2, Klf4 and cMyc[42] as previously described[43].

Growth assays. For BrdU incorporation assays, cells were incubated with 10 µM BrdU for 16–18 h and then fixed with 4% PFA (w/v). BrdU incorporation was assessed by IF and High Content Analysis microscopy. For crystal violet staining, the cells were seeded at low density on six-well dishes and fixed at the end of the treatment with 0.5% glutaraldehyde (w/v). The plates were then stained with 0.2% crystal violet (w/v).

IF staining of cells. Cells were grown in 96-well plates, fixed with 4% PFA (w/v), permeabilized in 0.2% Triton X-100 (v/v) diluted in PBS for 10 min and blocked with 1% BSA (w/v) and 0.4% fish gelatin (v/v) (Sigma) for 30 min. Cells were then incubated with a primary antibody for 45 min, followed by the corresponding fluorescence-labeled secondary antibody (AlexaFluor) for 30 min and 1 µg ml^{-1} DAPI for 15 min. Antibodies were diluted in blocking solution. After every step, cells were washed with PBS three times.

Cytochemical SA-β-galactosidase assay. Cells were grown in six-well plates, fixed with 0.5% glutaraldehyde (w/v) (Sigma) in PBS for 10–15 min, washed with 1 mM $MgCl_2$/PBS (pH 6.0) and then incubated with X-Gal staining solution (1 mg ml^{-1} X-Gal, Thermo Scientific, 5 mM $K_3[Fe(CN)_6]$ and 5 mM $K_4[Fe(CN)_6]$) for 8 h at 37 °C. Brightfield images of cells were taken using the DP20 digital camera attached to the Olympus CKX41 inverted light microscope. The percentage of SA-β-gal-positive cells was estimated by counting at least 100 cells per replicate sample facilitated by the 'point picker' tool of ImageJ software (National Institutes of Health)[44].

High content analysis. IF imaging was carried out using the automated high-throughput fluorescent microscope IN Cell Analyzer 2000 (GE Healthcare) with a ×20 objective, except for DNA damage foci analysis, which required a ×40 objective. Fluorescent images were acquired for each of the fluorophores using built-in wavelength settings ('DAPI' for DAPI, 'FITC' for AlexaFluor488 FITC and 'Texas Red' for AlexaFluor594). Multiple fields within a well were acquired to include a minimum of 1,000 cells per sample well. High content analysis of the images was conducted using INCell Investigator v.2.7.3 software. Briefly, DAPI served as a nuclear mask allowing for segmentation of cells with a TopHat method. To detect cytoplasmic staining in cultured cells, a collar of 7–9 µm around DAPI was applied.

Gene expression analysis. Total RNA was extracted using Trizol reagent (Invitrogen) and the RNeasy isolation kit (QIAGEN). Complementary DNA was generated using random hexamers and SuperScript II reverse transcriptase (Invitrogen). Quantitative real-time PCR was performed using SYBR Green PCR master mix (Applied Biosystems) in a CFX96 real-time PCR detection system (Bio-Rad). *RPS14* expression was used for normalization.

Human primer pairs were:

AHCY: ATTCCGGTGTATGCCTGGAAG, GAGATGCCTCGGATGCCTG.

p16^{INK4a}: CGGTCGGAGGCCGATCCAG, GCGCCGTGGAGCAGCAGCAGCT.

p15^{INKB}: GAATGCGCGAGGAGAACAAG, CCATCATCATGACCTGGATCG.

IL8: GAGTGGACCACACTGCGCCA, TCCACAACCCTCTGCACCCAGT.

IL1α: AGTGCTGCTGAAGGAGATGCCTGA, CCCCTGCCAAGCACACCCAGTA.

NSD2: ACCGCGAGTGTTCTGTGTTC, GTCGTGGCCGTTAAACTTCTG.

NSD3: AACTCATTGACTCCGCCAACA, CTGAAAGCCTTGCTGCAAAGT.

SMYD2: TACTGCAATGTGGAGTGTCAGA, ACAGTCTCCGAGGGATTCCAG.

RPS14: CTGCGAGTGCTGTCAGAGG, TCACCGCCCTACACATCAAACT.

Immunoblot. Histones were isolated using EpiQuik Total Histone Extraction kit (Epigentek, OP-0006) according to manufacturer's instructions. Immunoblotting was carried out using standard techniques as described before[15]. Uncropped blots are shown as source data for their corresponding figures.

Ex vivo culture of mouse satellite cells. C57BL/6 (WT) mice were bred and aged at the animal facility of the PRBB, housed in standard cages under 12-h light–dark cycles and fed ad libitum with a standard chow diet. Isolation of mouse stem cells for ex vivo culture was approved by the ethics committee of the PRBB and by the Catalan Government following applicable legislation. Both male and female mice were used in each experiment unless stated otherwise. Live colonies were maintained and genotyped as per Jackson Laboratory guidelines and protocols. Mice were housed together, health was monitored daily for sickness symptoms (such as non-age-related weight loss) and mice were killed immediately at the clinical end point when recommended by veterinary and biological services staff members. The mice determined by the animal facility veterinary team as healthy were used in the experiments. Mice determined as not healthy were excluded. No statistical methods were used to pre-determine the sample size, but our sample sizes are similar to those reported in previous publications[14,27]. The experiments were not randomized. Satellite cells from skeletal muscle from young (2–3 months old) or geriatric (28–31 months old) mice were isolated by FACS (based on α7-integrin and CD34 and negative selection) and cultured in growth medium (Ham's F10 supplemented with 20% FBS and bFGF (0.025 µg ml^{-1})) for 7 d. Proliferation assays (BrdU incorporation and staining) and senescent cell analysis (SA-β-gal assay, determination of RNA expression of *p16^{INK4a}*, *Cdkn1a*, *Myog* and *Myh3*; and γH2AX immunostaining), were performed after treatments of satellite cells with either vehicle (DMSO), rapamycin (100 ng ml^{-1}) for 48 h or 3DA (10 µM) for 6 d. All ex vivo experiments derived from animal tissue were approved by the Catalan Government (Spain).

For BrdU incorporation assays, cultured satellite cells were labeled with BrdU (1.5 µg ml^{-1}; Sigma) for 1 h and fixed with formaldehyde 3.7%. BrdU-labeled cells were detected by immunostaining using rat anti-BrdU antibody (1:500 dilution) and a specific secondary biotinylated goat anti-rat antibody (712-066-150 Jackson Immunoresearch; 1:250 dilution). Antibody binding was visualized using Vectastain Elite ABC reagent (Vector Laboratories) and DAB. BrdU-positive cells were quantified as percentage of the total number of cells analyzed.

SA-β-gal activity was detected in satellite cells using the Senescence β-Galactosidase Staining kit (Cell Signaling), according to the manufacturer's instructions. SA-β-gal$^+$ cells were quantified as percentage of the total number of cells analyzed.

For gene expression analysis, total RNA was isolated from cultured satellite cells of mouse muscle tissue, using an RNeasy Micro kit (QIAGEN) and analyzed by RT–qPCR. Real-time PCR reactions were performed on a Light Cycler 480 System using Light Cycler 480 SYBR Green I Master reaction mix (Roche Diagnostic Corporation) and specific primers. Thermocycling conditions were as follows: initial step of 10 min at 95 °C, then 50 cycles of 15 s, denaturation at 94 °C, 10 s annealing at 60 °C and 15 s extension at 72 °C. Reactions were run in triplicate and automatically detected threshold cycle values were compared between samples. Transcript of the ribosomal protein L7 housekeeping gene was used as endogenous control, with each unknown sample normalized to L7 content.

Mouse primer pairs were:

L7 (housekeeping): GAAGCTCATCTATGAGAAGGC, AAGACGAAGGAGCTGCAGAAC.

p16^{INK4a}: CATCTGGAGCAGCATGGAGTC, GGGTACGACCGAAAGAGTTCG.

Cdkn1a: CCAGGCCAAGATGGTGTCTT, TGAGAAAGGATCAGCCATTGC.

Myog: GGTGTGTAAGAGGAAGTCTGTG, TAGGCGCTCAATGTACTGGAT.

Myh3: AACAGAAACGCAATGCTGAGG, CAGCTCTCTGATCCGTGTCTC.

To assess DNA damage, cultured satellite cells were immunostained using a phospho-histone H2A.X (Ser139) antibody (1:50 dilution; Cell Signaling, 2577S). Digital images were acquired using a Leica SP5 confocal laser-scanning microscope with HCX PL Fluotar ×40/0.75.

Muscle regeneration. Mice were anesthetized with ketamine and xylazine (80 and 10 mg kg^{-1} intraperitoneally, respectively). Regeneration of skeletal muscle was induced by intramuscular injection of cardiotoxin (Latoxan, L8102; 10 µM) as described elsewhere[45]. At the indicated days post-injury, mice were killed and muscles were dissected, frozen in liquid nitrogen-cooled isopentane and stored at −80 °C until analysis[27].

Satellite cell transplantation. Transplantation of satellite cells was performed as described elsewhere[14] following an adapted protocol[46]. Satellite cells from young or geriatric mice (treated with the indicated compounds or vehicle ex vivo) were resuspended in 20% FBS HAMF10 medium, labeled with Vybrant Dil Cell Labeling solution (Dil) (Invitrogen, V22889) according to the manufacturer's instructions and injected into tibialis anterior muscles of recipient immunodeficient mice previously injured with freeze crush[47] 1 d before. For better comparison of untreated versus 3DA-treated geriatric satellite cells, engraftment of both conditions was performed within the same host mice, using one tibialis anterior muscle for untreated cells and the contralateral one for 3DA-treated satellite cells. Each muscle was engrafted with 10,000 cells. Investigators were not blinded to allocation and outcome assessment for the satellite cell transplantation experiment, as engraftment of both conditions was performed within the same host mouse. Muscles were collected and processed for muscle histology 5 d after cell transplantation. For GFP-labeling experiments, freshly isolated satellite cells from young or geriatric mice were treated with vehicle or 3DA for 4 d, transduced with a GFP lentivirus (pCCLsin.PPT.hPGK.GFPpre, 5.6×10^8 transduction units per ml) and engrafted into tibialis anterior muscles of recipient immunodeficient mice previously injured with freeze crush[47] 1 d before. Muscles were collected 6 d after engraftment and GFP$^+$ fibers were analyzed.

Muscle histology. Muscles were embedded in OCT solution (TissueTek, 4583), frozen in isopentane cooled with liquid nitrogen and stored at −80 °C until analysis. The 10 µm muscle cryosections were collected and stained for SA-β-gal (AppliChem, A1007,0001). The number of SA-β-gal$^+$ cells was quantified using ImageJ software. For GFP immunostaining, the muscle was prefixed 2 h in PFA 2% at 4 °C, embedded in sucrose 30% O/N at 4 °C and then frozen in liquid nitrogen-cooled isopentane. The 8–10 µm sections were collected from muscles and double immunostaining was performed as followed. Sections were air-dried, washed on PBS and incubated with primary antibody according to the manufacturer's instructions after blocking for 1 h at room temperature in a high-protein-containing solution (goat serum) in PBS. Subsequently, slides were washed in PBS and incubated with a secondary antibody and labeling dye and nuclei were stained with DAPI (Invitrogen). After washing, tissue sections were mounted with Fluoromount G (SouthernBiotech, 0100-01). Digital images were acquired using a Zeiss Cell Observer HS with ×20 air objective and a Zeiss AxioCam MrX camera. The acquisition was performed using Zeiss LSM software Zen.

Two-third hepatectomy. Six-month-old female C57BL/6JInv mice were purchased from InVivos and were kept until 2 years old. Mice were housed in BRC in specific-pathogen-free conditions under a 12-h light–dark cycle with lights turned off at 19:00 and resumed at 7:00. The animals were housed in individually ventilated cages maintained at ~21 °C and 60–65% relative humidity. Two-thirds (partial) hepatectomy (2/3 PH) was performed on 2-year-old C57BL6/J WT mice as described before[48]. No statistical methods were used to pre-determine sample sizes, but our sample sizes are similar to those reported in a previous publication[49]. All animals were randomly allocated into a carrier ($n=4$) or treatment ($n=4$) group but, for each experimental condition, one mouse did not survive the operation. Therefore the 'day 2' Ki67 analysis was carried out with three mice per group ($n=3$). The histopathology analysis was performed at day 0 on paraffin sections and includes $n=4$ per group. The γH2AX IF was performed at day 0 on frozen sections. There were issues with the integrity of the frozen sections of one of the 3DA-treated mice, so for the γH2AX IF, the carrier group was $n=4$ and the treatment group *was* $n=3$. The median, right and caudate liver lobes were surgically removed (day 0 time point) while mice were under general isoflurane anesthesia. At 48 h later, the remaining liver was collected and further analyzed. Microscopic analyses were performed using an Observer Z1 microscope (Zeiss). Five high-power fields were counted on two liver sections (from OCT-embedded cryo-frozen tissue) from each mouse liver (×20, >200 counted cells per field). Histopathological evaluation of murine livers was performed on hematoxylin and eosin (H&E)-stained paraffin sections by board-certified pathologists (Advanced Molecular Pathology Laboratory, Institute of Molecular and Cell Biology and BRC A*STAR, Singapore). The severity of changes, where applicable, was graded as follows: NAD, no abnormalities detected; grade 1, minimal; grade 2, mild; grade 3, moderate; grade 4, marked; and grade 5, severe. Staining and counting were performed in a blinded fashion, the investigator was not aware to which group the animal belonged.

Isolation of cord blood-derived hematopoietic stem and progenitor cells. To obtain CD34$^+$ HSPCs, human male and female cord blood samples were acquired from healthy full-term pregnancies (Obstetrics Department at the Isala Hospital in Zwolle, The Netherlands) after written informed consent, in accordance with the Declaration of Helsinki. CD34$^+$ HSPCs were isolated as previously described[50]. Briefly, CD34$^+$ HSPC cord blood was diluted 1:1 with PBS + 2 mM EDTA + 0.5% v/v BSA (PBS/EDTA/BSA) and layered on Lymphoprep (Stem Cell Technologies). After centrifugation for 20 min at 800*g*, without brakes, the middle layer containing mononuclear cells was collected. These cells were resuspended in PBS/EDTA/BSA and then centrifuged for 5 min at 800*g*. Cell pellets were collected, washed with PBS/EDTA/BSA and centrifuged for 10 min at 200*g*. Immunomagnetic labeling and separation were performed according to the manufacturer's manual of the CD34 MicroBead kit, human (Miltenyi Biotec).

Long-term culture-initiating cell assay. CD34$^+$ cells were sorted at a limiting dilution directly onto 96-well plates on a feeder layer of MS5 cells (DSMZ, ACC441) in Myelocult H5100 (Stem Cell Technologies) supplemented with 10^{-6} M hydrocortisone (Stem Cell Technologies) and 1% v/v penicillin–streptomycin–glutamine (100×) (Gibco). Cells were cultured for 5 weeks with 10 µM 3DA or vehicle (DMSO) and half-medium changes were performed weekly. After 5 weeks the medium was replaced by Methocult H4335 (Stem Cell Technologies) and incubated for 2 weeks more at 37 °C and 5% CO_2. Colony formation was assessed by phase-contrast microscopy after 7 weeks. The LTC-IC frequency of each experiment was calculated with ELDA software[51].

Culture of cord-blood-derived HSPCs. Cord-blood-derived HSPCs were cultured in Stemspan (Stem Cell Technologies) supplemented with 1% v/v penicillin–streptomycin–glutamine (100×) (Gibco) and the cytokines FLT3L, TPO and SCF (R&D Systems) all at a concentration of 100 ng ml^{-1}. The cells were seeded at a starting density of 250,000 cells ml^{-1} and treated with 10 µM 3DA or vehicle (DMSO) on days 1, 4 and 7. Cells were cultured in a humidified atmosphere of 5% CO_2 at 37 °C. Cells were collected and counted manually with a hemocytometer and trypan blue at day 9. Cells were analyzed by FACS and used for RNA-seq and xenotransplantation. The percentage of CD34$^+$CD38$^+$ cells was determined after blocking with Fc block (BD) for 10 min at room temperature and incubation with CD34$^+$ PE-Cy7 (BD, 348811) and CD38$^+$ FITC (BD, 555459) for 20–25 min at 4 °C in the dark. Afterward, cells were washed and resuspended with PBS + BSA 0.2% containing a viability dye (Propidium iodide (PI)). Samples were analyzed on a FACSCanto II (BD).

RNA-seq of human umbilical cord-blood cells. CD34$^+$CD38$^-$ cells were obtained from cord blood cells (from four different donors: 338, 522, 535 and 545) that had been treated for 9 d with DMSO (DMSO) or 10 µM 3DA, sorted using FACS and subjected to RNA-seq. The sequencing was conducted on an Illumina NextSeq 500 system with 41-bp paired-end reads. Base calling was performed during the sequencing run by Real-Time Analysis v.2.11.3 running under NextSeq 500 Control Software v.4.0.2. CASAVA-2.17 was used for secondary analysis.

Xenotransplantation. Mouse experiments were performed in line with international and national guidelines. All experiments were approved by the IACUC RUG. Mice were kept in sterile conditions in individually ventilated filter-top cages at 20 °C under 12-h dark–light cycles. For all xenotransplantation studies we performed single cord transplantations of freshly isolated CD34$^+$ cord blood cells into 2–3 mice per condition. Recipient mice were randomly assigned to an experimental group. Cord blood samples were selected that contained sufficient numbers of CD34$^+$ cells to carry out the experiments. No statistical methods were used to pre-determine sample sizes but our sample sizes are similar to those reported previously[50]. Female 10–25-week-old NOD.Cg-Prkdcscid Il2rgtm1Wjl/SzJ mice were radiated 3 h before transplantation with 1.8 Gy. In each experiment, the age of mice was balanced between the experimental and control group with a maximum difference of 9 d. In total, equivalents of 1.5×10^6 cells pre-treated for 9 d with 3DA or the vehicle (DMSO) were transplanted per mouse via retro-orbital injection under general anesthesia. No animals were excluded from the analysis. Data collection and analysis were not performed blind to the conditions of the experiments.

Bleeding and bone-marrow analysis of xenotransplanted NSG mice. Beginning 6 weeks after transplantation, chimerism in peripheral blood was determined in 4-week intervals. Blood samples were taken under general anesthesia via retro-orbital bleeding. Mice were killed between week 18 and 31 and dissected under general anesthesia after the end of the experiment or reaching the humane end point of the experiment. Bones (femur, tibia, fibula and pelvis) were collected and cleaned. Bones were crushed in the presence of PBS + 0.2% PBS with a mortar and pestle. The obtained cell suspension was filtered through a 40 µm filter. Remaining erythrocytes were lysed with ammonium chloride. Cells were then washed twice with PBS + BSA 0.2%, pelleted by centrifugation and resuspended in BV stain buffer (BD). Samples were incubated with Human Fc block (BD) and CD16/CD32 Mouse Fc block (BD) to prevent unspecific binding. After incubation for 10 min at room temperature antibody master mix was added and samples were incubated for 20–25 min at 4 °C in the dark. The antibody mix contained CD3-APC-Cy7 (BioLegend, 344818), CD19-PE (BD, 561741), CD33-BV421 (BD, 562854), CD45-APC (BD, 555485) for the bleeding and for bone-marrow analysis also CD38-FITC (BD, 555459), CD34-PE-Cy7 (BD, 348811) and CD90-BV605 (BD, 562685) (or CD38-BV605 (BD, 562665) and no CD90 for experiment A and D). Afterward, cells were washed and resuspended with PBS + BSA 0.2% containing a viability dye (PI). Samples were analyzed on an LSR II (BD) or FACSCanto II (BD).

Flow cytometry analysis. All flow cytometry measurements were analyzed using FlowJo (v.7). Dead cells were excluded from the analysis by gating out lower forward scatter and high DAPI or PI-retaining cells. All statistical analyses were performed using GraphPad Prism v.6 (GraphPad Software) or R (R Foundation for Statistical Computing). Gating strategies are shown in Extended Data Fig. 10g,h.

RNA-seq analysis. RNA-seq libraries were prepared from 30 ng of total RNA using the Nextera XT DNA sample preparation and dual indexing kits (Illumina) according to the manufacturer's protocol with a few modifications as previously described[43,52]. Library quality was checked on a Bioanalyser HS DNA chip and concentrations were estimated by Qubit measurement. Libraries were pooled in equimolar quantities and sequenced on a Hiseq2500 using single-end 50-bp reads. At least 20 million reads passing the filter were achieved per sample. Sequencing reads from the RNA-seq experiments were aligned to the hg19 genome using TopHat v.2.0.11 (ref. [53]) using parameters '–library-type fr-firststrand–b2-very-sensitive–b2-L 25' and using known transcripts annotation from Ensembl gene v.72. Number of reads counts on exons were summarized using HTSeq v.0.5.3p9 with '–stranded=reverse' option and differentially expressed genes were identified using DESeq2 (ref. [54]). Genes were ranked by fold change and GSEA was performed using the GSEA v.2.07 (Broad Institute) pre-ranked module.

H3K36me3 histone modification ChIP-seq. A total of 1×10^7 cells were fixed in 1% formaldehyde for 15 min, quenched in 2 M glycine for an additional 5 min and pelleted by centrifugation at 425*g*, 4 °C for 4 min[55]. For H3K36me3 histone

modification ChIP-seq, nuclei were extracted in extraction buffer 2 (0.25 M sucrose, 10 mM Tris-HCl, pH 8.0, 10 mM $MgCl_2$, 1% Triton X-100 and proteinase inhibitor cocktail) on ice for 10 min followed by centrifugation at 3,000*g* at 4 °C for 10 min. The supernatant was removed and nuclei were resuspended in nuclei lysis buffer (50 mM Tris-HCl, pH 8.0, 10 mM EDTA and 1% SDS and proteinase inhibitor cocktail). Sonication was performed using a Diagenode Picoruptor until the desired average fragment size (100–500 bp) was obtained. Soluble chromatin was obtained by centrifugation at 14,046*g* for 10 min at 4 °C and chromatin was diluted tenfold. Immunoprecipitation was performed overnight at 4 °C with rotation using 1–2 × 10^6 cell equivalents per immunoprecipitation using 5 µg antibody against H3K36me3 (D5A7, Cell Signaling Technology, 4909). Subsequently, 30 µl of Ultralink Resin (Thermo Fisher Scientific) were added and allowed to tumble for 4 h at 4 °C. The resin was pelleted by centrifugation and washed three times in low-salt buffer (150 mM NaCl, 0.1% SDS, 1% Triton X-100, 20 mM EDTA and 20 mM Tris-HCl, pH 8.0), once in high-salt buffer (500 mM NaCl, 0.1% SDS, 1% Triton X-100, 20 mM EDTA and 20 mM Tris-HCl, pH 8.0), twice in lithium chloride buffer (250 mM LiCl, 1% IGEPAL CA-630, 15 sodium deoxycholate, 1 mM EDTA and 10 mM Tris-HCl, pH 8.0) and twice in TE buffer (10 mM Tris-HCl and 1 mM EDTA). DNA was recovered by mixing the de-crosslinked supernatant with 2.2× SPRI beads followed by 4 min of incubation at room temperature. SPRI beads were washed twice in 80% ethanol, allowed to dry and DNA was eluted in 35 µl of 10 mM Tris-Cl, pH 8.0. Libraries were constructed using the Accel-NGS 2S Plus DNA Library kit (Swift Biosciences, 21024) according to the manufacturer's instructions. Libraries were amplified for 12 cycles. Libraries were then resuspended in 20 µl of low EDTA–TE buffer and quality controlled in an Agilent Technologies 4200 Tapestation (G2991-90001) and quantified using an Invitrogen Qubit DS DNA HS Assay kit (Q32854). Libraries were sequenced using an Illumina High-Seq 2500. Typically, 30–50 million reads were required for downstream analyses.

ChIP-seq analysis. Reads were cleaned and trimmed using fastq-mcf from the ea-utils suite v.1.1.2 to remove adaptors, low-quality bases and reads and discard reads shorter than 25 bp after filtering. Reads were then aligned to the human reference genome (hg19) with bowtie v.1.1.1 using best matches parameters (bowtie -v 2 -m 1–best–strata). Alignment files were further processed with samtools v.1.2 and PicardTools v.1.130 to flag PCR and optical duplicates and remove alignments located in Encode blacklisted regions. Fragment size was estimated in silico for each library using spp v.1.10.1. Genome-wide consistency between replicates was checked using custom R scripts. Enriched regions were identified for each replicate independently with MACS v.2.1.0 with non-IPed genomic DNA as a control (macs2 callpeak–nomodel–shiftsize–shift-control–gsize hs -p 1e-1). These relaxed peak lists were then processed through the irreproducible discovery rate pipeline to generate an optimal and reproducible set of peaks for each histone modification and each time point. After assessing library saturation using preseqR, alignment and peak data were imported and pre-processed in R using the DiffBind package. We counted the number of reads mapping inside the global set of irreproducible discovery rate reproducible peaks for each condition and for each replicate. The raw count matrix was then normalized for sequencing depth using a non-linear full quantile normalization as implemented in the EDASeq package. To remove sources of unwanted variation and consider batch effects, data were finally corrected with the RUVSeq package. Differential analyses for count data were performed using edgeR considering condition and batch in the design matrix, by fitting a negative binomial generalized log-linear model to the read counts for each peak. Peaks were finally annotated using ChIPpeakAnno considering annotations provided by Ensembl v.86. For combined ChIP-seq/RNA-seq analysis, RNA-seq reads were assigned to genes using featureCounts from Rsubread package. The count matrix was processed as previously described for the ChIP-seq data. Statistical analyses was also performed as described for ChIP-seq data.

Statistics and reproducibility. GraphPad Prism 8 was used for statistical analysis. Data distribution was assumed to be normal but this was not formally tested. Two-tailed, unpaired, Student's *t*-tests were used to estimate statistically significant differences between two groups. Two-way ANOVA with Tukey's post-hoc comparison was used for multiple comparisons. Values are presented as mean ± s.d. unless otherwise indicated.

For the cord blood in vivo studies, mice were stratified to treatment groups based on age and cage. All four experiments in the present study represent separate cord blood samples from which cells from each condition were transplanted into 2–3 mice, all replicates indicate individual mice. Mice with engraftment <1% were not included in further analysis.

Reporting summary. Further information on research design is available in the Nature Research Reporting Summary linked to this article.

Data availability

Source data is included with this paper. The RNA-seq and ChIP-seq data generated in the present study have been deposited in the Gene Expression Omnibus database under accession nos. GSE155906 and GSE175770.

Code availability

All software and packages used are listed in the Reporting Summary and are publicly available. The code relevant to the ChIP-seq analysis is hosted on Zenodo (https://zenodo.org, https://doi.org/10.5281/zenodo.6865749).

Received: 25 August 2020; Accepted: 4 August 2022;
Published online: 13 September 2022

References

1. Gorgoulis, V. et al. Cellular senescence: defining a path forward. *Cell* **179**, 813–827 (2019).
2. Salama, R., Sadaie, M., Hoare, M. & Narita, M. Cellular senescence and its effector programs. *Genes Dev.* **28**, 99–114 (2014).
3. Collado, M. et al. Tumour biology: senescence in premalignant tumours. *Nature* **436**, 642 (2005).
4. Krizhanovsky, V. et al. Senescence of activated stellate cells limits liver fibrosis. *Cell* **134**, 657–667 (2008).
5. Munoz-Espin, D. & Serrano, M. Cellular senescence: from physiology to pathology. *Nat. Rev. Mol. Cell Biol.* **15**, 482–496 (2014).
6. Baker, D. J. et al. Naturally occurring p16(Ink4a)-positive cells shorten healthy lifespan. *Nature* **530**, 184–189 (2016).
7. Ovadya, Y. & Krizhanovsky, V. Strategies targeting cellular senescence. *J. Clin. Invest.* **128**, 1247–1254 (2018).
8. Lapasset, L. et al. Rejuvenating senescent and centenarian human cells by reprogramming through the pluripotent state. *Genes Dev.* **25**, 2248–2253 (2011).
9. Latorre, E. et al. Small molecule modulation of splicing factor expression is associated with rescue from cellular senescence. *BMC Cell Biol.* **18**, 31 (2017).
10. Georgilis, A. et al. PTBP1-mediated alternative splicing regulates the inflammatory secretome and the pro-tumorigenic effects of senescent cells. *Cancer Cell* **34**, 85–102 (2018).
11. Xu, M. et al. JAK inhibition alleviates the cellular senescence-associated secretory phenotype and frailty in old age. *Proc. Natl Acad. Sci. USA* **112**, E6301–E6310 (2015).
12. Krishnamurthy, J. et al. p16INK4a induces an age-dependent decline in islet regenerative potential. *Nature* **443**, 453–457 (2006).
13. Molofsky, A. V. et al. Increasing p16INK4a expression decreases forebrain progenitors and neurogenesis during ageing. *Nature* **443**, 448–452 (2006).
14. Sousa-Victor, P. et al. Geriatric muscle stem cells switch reversible quiescence into senescence. *Nature* **506**, 316–321 (2014).
15. Guerrero, A. et al. Cardiac glycosides are broad-spectrum senolytics. *Nat Metab.* **1**, 1074–1088 (2019).
16. Chiang, P. K. Biological effects of inhibitors of *S*-adenosylhomocysteine hydrolase. *Pharmacol. Ther.* **77**, 115–134 (1998).
17. De La Haba, G. & Cantoni, G. L. The enzymatic synthesis of *S*-adenosyl-L-homocysteine from adenosine and homocysteine. *J. Biol. Chem.* **234**, 603–608 (1959).
18. Acosta, J. C. et al. A complex secretory program orchestrated by the inflammasome controls paracrine senescence. *Nat. Cell Biol.* **15**, 978–990 (2013).
19. Jacobs, J. J. & de Lange, T. Significant role for p16INK4a in p53-independent telomere-directed senescence. *Curr. Biol.* **14**, 2302–2308 (2004).
20. Innes, A. J. et al. XPO7 is a tumor suppressor regulating p21(CIP1)-dependent senescence. *Genes Dev.* **35**, 379–391 (2021).
21. d'Adda di Fagagna, F. et al. A DNA damage checkpoint response in telomere-initiated senescence. *Nature* **426**, 194–198 (2003).
22. Chiang, P. K. & Cantoni, G. L. Perturbation of biochemical transmethylations by 3-deazaadenosine in vivo. *Biochem. Pharmacol.* **28**, 1897–1902 (1979).
23. Tan, J. et al. Pharmacologic disruption of Polycomb-repressive complex 2-mediated gene repression selectively induces apoptosis in cancer cells. *Genes Dev.* **21**, 1050–1063 (2007).
24. Wagner, E. J. & Carpenter, P. B. Understanding the language of Lys36 methylation at histone H3. *Nat. Rev. Mol. Cell Biol.* **13**, 115–126 (2012).
25. Hou, P. et al. Pluripotent stem cells induced from mouse somatic cells by small-molecule compounds. *Science* **341**, 651–654 (2013).
26. Banito, A. et al. Senescence impairs successful reprogramming to pluripotent stem cells. *Genes Dev.* **23**, 2134–2139 (2009).
27. Garcia-Prat, L. et al. Autophagy maintains stemness by preventing senescence. *Nature* **529**, 37–42 (2016).
28. Scarpa, S. et al. Differentiation of myoblast cell lines and biological methylation: 3-deazaadenosine stimulates formation of multinucleated myofibers. *Proc. Natl Acad. Sci. USA* **81**, 3064–3068 (1984).
29. Sousa-Victor, P., Garcia-Prat, L. & Munoz-Canoves, P. Control of satellite cell function in muscle regeneration and its disruption in ageing. *Nat. Rev. Mol. Cell Biol.* **23**, 204–226 (2022).
30. Kwon, S. M., Hong, S. M., Lee, Y. K., Min, S. & Yoon, G. Metabolic features and regulation in cell senescence. *BMB Rep.* **52**, 5–12 (2019).

31. Yang, S. et al. Oval cells compensate for damage and replicative senescence of mature hepatocytes in mice with fatty liver disease. *Hepatology* **39**, 403–411 (2004).
32. Fausto, N. & Campbell, J. S. The role of hepatocytes and oval cells in liver regeneration and repopulation. *Mech. Dev.* **120**, 117–130 (2003).
33. Broxmeyer, H. E. Enhancing the efficacy of engraftment of cord blood for hematopoietic cell transplantation. *Transfus. Apher. Sci.* **54**, 364–372 (2016).
34. Brunstein, C. G. & Wagner, J. E. Cord blood transplantation for adults. *Vox. Sang.* **91**, 195–205 (2006).
35. Baker, D. J. et al. Clearance of p16Ink4a-positive senescent cells delays ageing-associated disorders. *Nature* **479**, 232–236 (2011).
36. Tanaka, H. et al. The NSD2/WHSC1/MMSET methyltransferase prevents cellular senescence-associated epigenomic remodeling. *Aging Cell* **19**, e13173 (2020).
37. Mosteiro, L. et al. Tissue damage and senescence provide critical signals for cellular reprogramming in vivo. *Science* **354**, aaf4445 (2016).
38. Chiche, A. et al. Injury-Induced Senescence Enables In Vivo Reprogramming in Skeletal Muscle. *Cell Stem Cell* **20**, 407–414 (2017).
39. Boitano, A. E. et al. Aryl hydrocarbon receptor antagonists promote the expansion of human hematopoietic stem cells. *Science* **329**, 1345–1348 (2010).
40. Fares, I. et al. Cord blood expansion. Pyrimidoindole derivatives are agonists of human hematopoietic stem cell self-renewal. *Science* **345**, 1509–1512 (2014).
41. Gupta, R. et al. Nov/CCN3 enhances cord blood engraftment by rapidly recruiting latent human stem cell activity. *Cell Stem Cell* **26**, 527–541 (2020).
42. Carey, B. W. et al. Reprogramming of murine and human somatic cells using a single polycistronic vector. *Proc. Natl Acad. Sci. USA* **106**, 157–162 (2009).
43. Aarts, M. et al. Coupling shRNA screens with single-cell RNA-seq identifies a dual role for mTOR in reprogramming-induced senescence. *Genes Dev.* **31**, 2085–2098 (2017).
44. Guerrero, A. et al. Galactose-modified duocarmycin prodrugs as senolytics. *Aging Cell* **19**, e13133 (2020).
45. Suelves, M. et al. uPA deficiency exacerbates muscular dystrophy in MDX mice. *J. Cell Biol.* **178**, 1039–1051 (2007).
46. Sacco, A. et al. Short telomeres and stem cell exhaustion model Duchenne muscular dystrophy in mdx/mTR mice. *Cell* **143**, 1059–1071 (2010).
47. Le, G., Lowe, D. A. & Kyba, M. Freeze injury of the tibialis anterior muscle. *Methods Mol. Biol.* **1460**, 33–41 (2016).
48. Mitchell, C. & Willenbring, H. A reproducible and well-tolerated method for 2/3 partial hepatectomy in mice. *Nat. Protoc.* **3**, 1167–1170 (2008).
49. Loforese, G. et al. Impaired liver regeneration in aged mice can be rescued by silencing Hippo core kinases MST1 and MST2. *EMBO Mol. Med.* **9**, 46–60 (2017).
50. Jung, J. et al. CBX7 induces self-renewal of human normal and malignant hematopoietic stem and progenitor cells by canonical and non-canonical interactions. *Cell Rep.* **26**, 1906–1918 (2019).
51. Hu, Y. & Smyth, G. K. ELDA: extreme limiting dilution analysis for comparing depleted and enriched populations in stem cell and other assays. *J. Immunol. Methods* **347**, 70–78 (2009).
52. Picelli, S. et al. Full-length RNA-seq from single cells using Smart-seq2. *Nat. Protoc.* **9**, 171–181 (2014).
53. Trapnell, C., Pachter, L. & Salzberg, S. L. TopHat: discovering splice junctions with RNA-Seq. *Bioinformatics* **25**, 1105–1111 (2009).
54. Love, M. I., Huber, W. & Anders, S. Moderated estimation of fold change and dispersion for RNA-seq data with DESeq2. *Genome Biol.* **15**, 550 (2014).
55. Martinez-Zamudio, R. I. et al. AP-1 imprints a reversible transcriptional programme of senescent cells. *Nat. Cell Biol.* **22**, 842–855 (2020).

Acknowledgements

We are grateful to members of J. Gil's laboratory for reagents, comments and other contributions to this project. We thank members of the Genomics LMS facility (L. Game, K. Rekopoulou and A. Ivan) and the Bioinformatics LMS facility (G. Dharmalingam, M. Karimi and H. Pallikonda) for help with RNA-seq and data processing. We thank O.C. Bing (BRC, A*STAR) for the histopathology scoring of liver sections. For the purpose of open access, the author has applied a Creative Commons Attribution license. Core support from MRC (MC_U120085810), a Development Gap Fund grant from LifeArc and Cancer Research UK (C15075/A28647) funded this research in J. Gil's laboratory. P.M.-C. acknowledges funding from RTI2018-096068-B-I00, ERC-2016-AdG-741966, La Caixa HR17-00040, UPGRADE-H2020-825825, MWRF, Fundació La Marató-TV3, AFM, MDA and DPP-E. This work was supported by grants from the Deutsche Krebshilfe (to J.J.), the Dutch Cancer Society (to G.d.H.) and the Tekke Huizinga Fund (S.B. and G.d.H.). L.R. was supported by the Pasteur - Paris University International PhD Program and by the Fondation pour la Recherche Médicale. O.B was supported by Fondation ARC pour la Recherche sur le Cancer, INSERM-AGEMED and ANR S-ENCODE - 19-CE13-0017-01. O.B. is a Centre National de la Recherche Scientifique Research Director DR2. T.W. was funded by National Medical Research Council, Singapore through NMRC/OFLCG/003b/2018 and A*STAR through the Central Research Fund for Applied/Translational Research.

Author contributions

A.G. designed, performed and analyzed the cell culture experiments and wrote the first draft of the manuscript. A.J.I., V.W., M.A. and N.M. designed, performed and analyzed experiments. L.R. performed the ChIP-seq experiments. P.-F.R. analyzed the ChIP-seq and RNA-seq data. O.B. designed and analyzed the ChIP-seq experiments, secured funding and wrote the manuscript. S.C.B., J.J. and A.A. designed, performed and analyzed the UCB experiments. G.d.H. designed and analyzed the UCB experiments, secured funding and wrote the manuscript. L.O. and V.M. designed, performed and analyzed the muscle stem cell experiments. E.P. and P.M.-C. designed, analyzed and wrote the muscle stem cell experiments and secured funding. A.P. designed, performed and analyzed the liver regeneration experiments. T.W. designed, analyzed and wrote the liver regeneration experiments and secured funding. J.G. conceived and designed the project, secured funding and wrote the manuscript, with all authors providing feedback.

Competing interests

J.G. has acted as a consultant for Unity Biotechnology, Geras Bio, Myricx Pharma and Merck KGaA. Pfizer and Unity Biotechnology have funded research in J.G.'s laboratory (unrelated to the work presented here). J.G. owns equity in Geras Bio. J.G. and A.G. are named inventors in an MRC patent and J.G. is a named inventor in other Imperial College patents, both related to senolytic therapies (the patents are not related to the work presented here). T.W. is scientific co-founder of, and holds stakes in, Cargene Therapeutics, which develops nucleic-acid therapeutics for liver diseases (unrelated to the work presented here). The remaining authors declare no competing interests.

Additional information

Extended data is available for this paper at https://doi.org/10.1038/s43587-022-00279-9.

Supplementary information The online version contains supplementary material available at https://doi.org/10.1038/s43587-022-00279-9.

Correspondence and requests for materials should be addressed to Jesús Gil.

Peer review information *Nature Aging* thanks Richard Faragher, Valery Krizhanovsky and the other, anonymous, reviewer(s) for their contribution to the peer review of this work. Primary Handling Editor: Anna Kriebs, in collaboration with the *Nature Aging* team.

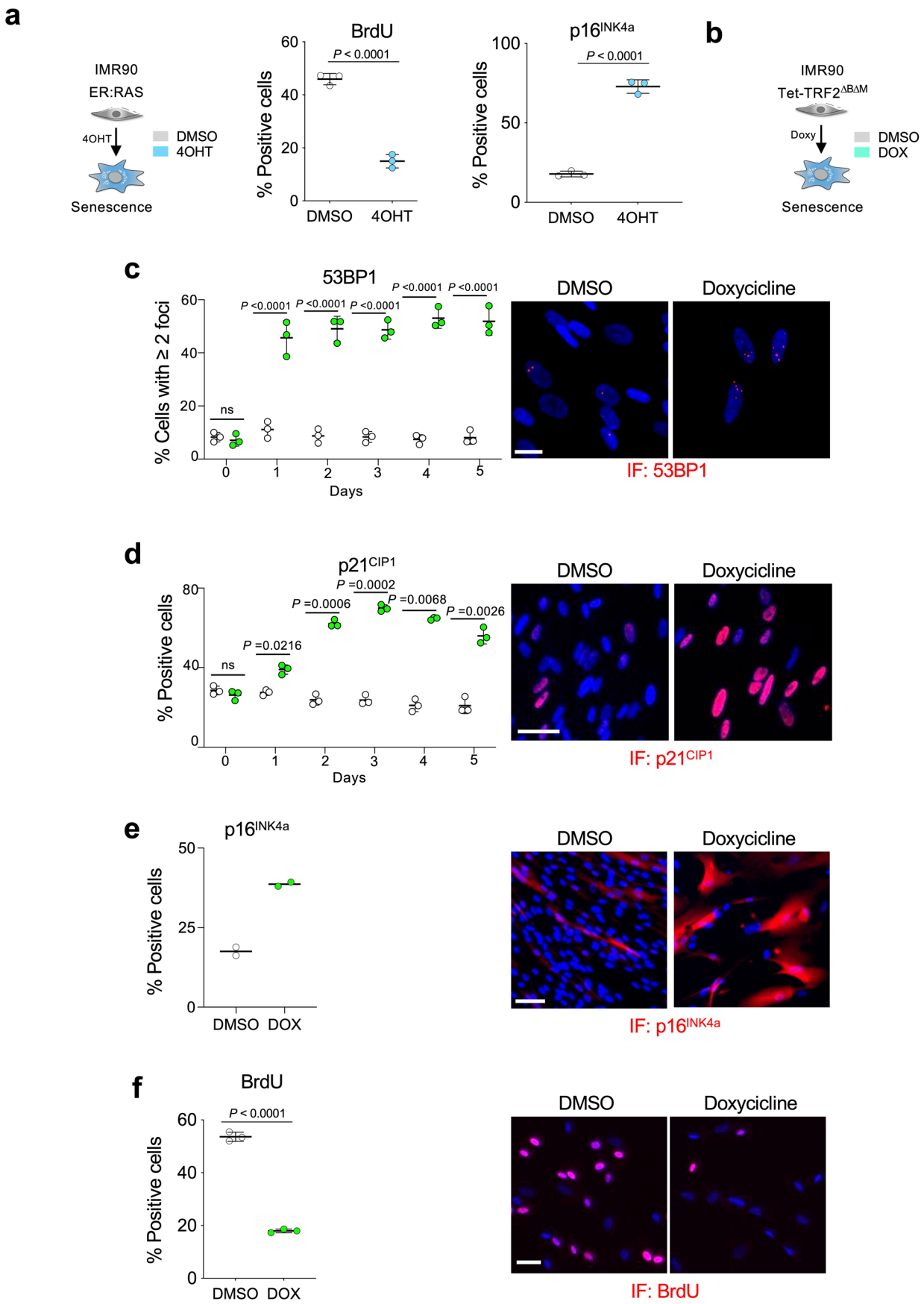

Extended Data Fig. 1 | See next page for caption.

Extended Data Fig. 1 | Cellular models of senescence induced by oncogene activation and telomere uncapping. a, IMR90 ER:RAS as a model of OIS. Quantification of immunofluorescence staining for BrdU (left) and $p16^{INK4a}$ (right) of IMR90 ER:RAS cells 4 days after treatment with 4OHT or vehicle (DMSO) ($n = 3$). **b**, IMR90 tet-$TRF2^{\triangle B\triangle M}$ as a model of telomere uncapping-induced senescence. **c**, Left, quantification of immunofluorescence staining for 53BP1 of IMR90 tet-$TRF2^{\triangle B\triangle M}$ cells after treatment with doxycycline or vehicle (DMSO) ($n = 3$). Right, representative immunofluorescence images. Scale bar, 20 μm. **d**, Left, quantification of immunofluorescence staining for $p21^{CIP1}$ ($n = 3$). Right, representative immunofluorescence images. Scale bar, 50 μm. **e**, Left, quantification of immunofluorescence staining for $p16^{INK4a}$ (day 7, $n = 2$). Right, representative immunofluorescence images. Scale bar, 100 μm. **f**, Left, quantification of immunofluorescence staining for BrdU (day 3, $n = 3$). Right, representative immunofluorescence images. Scale bar, 50 μm. All statistical significances were calculated using unpaired two-tailed *t*-tests. All error bars represent mean ± s.d; *n* represents independent experiments.

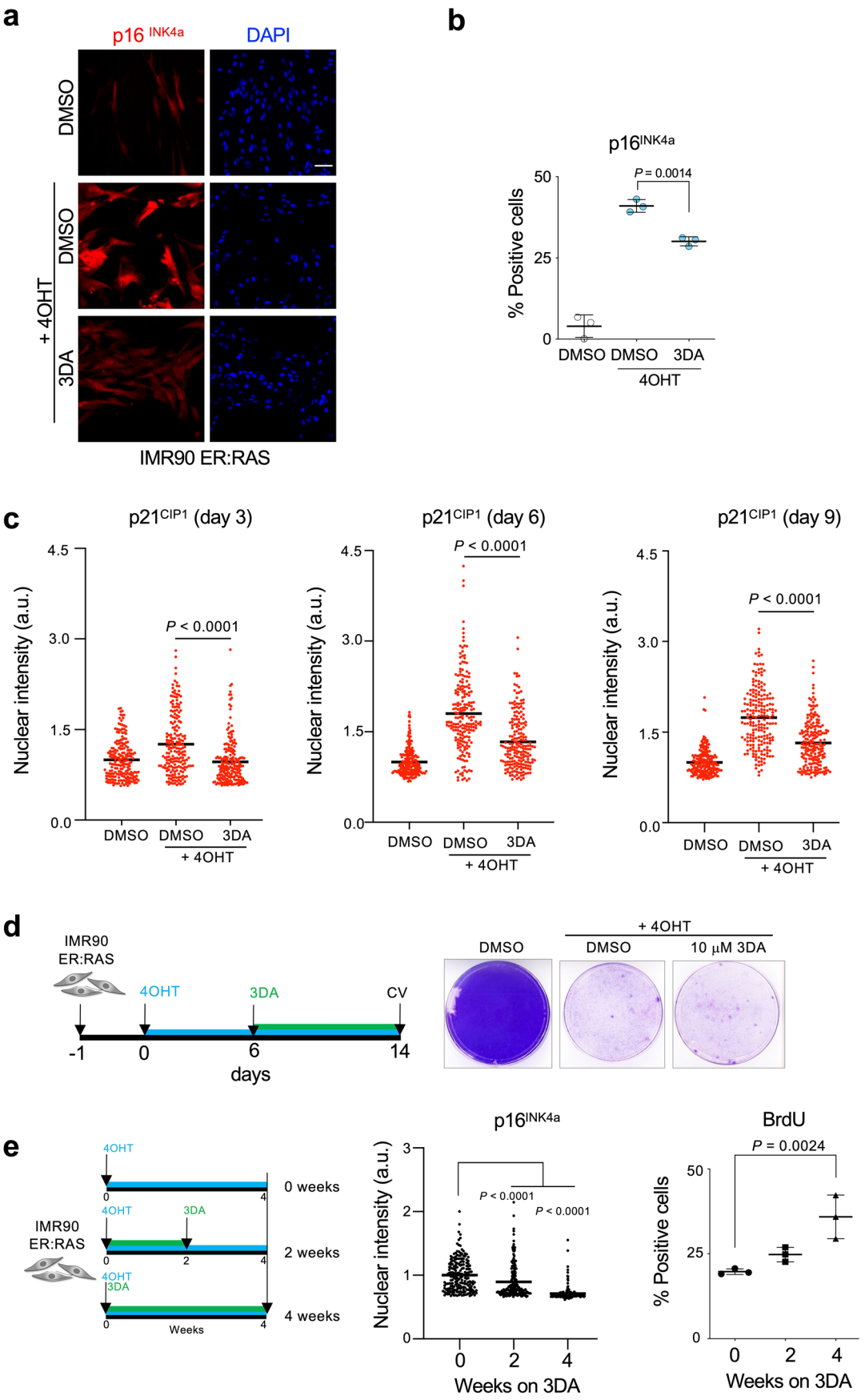

Extended Data Fig. 2 | See next page for caption.

Extended Data Fig. 2 | Treatment with 3DA alleviates oncogene-induced senescence. a, Representative immunofluorescence images of $p16^{INK4a}$ (red) in IMR90 ER:RAS cells cells 4 days after treatment with 4OHT and 10 μM 3DA or vehicle (DMSO). Scale bar, 100 μm. **b**, Quantification ($n = 3$). The statistical significance was calculated using unpaired two-tailed *t*-test. **c**, $p21^{CIP1}$ protein expression in IMR90 ER:RAS cells treated with DMSO or 4OHT to induce senescence or 4OHT and 10 μM 3DA. Normalized nuclear intensity values and mean values on day 3 (left), day 6 (middle) and day 9 (right panel) are shown ($n = 200$ cells per condition). The statistical significance was calculated using unpaired two-tailed *t*-tests. **d**, Timeline of the experiment (left) and crystal violet staining (right). IMR90 ER:RAS cells were treated with 4OHT continuously to induce senescence. On day 6, DMSO or 10 μM 3DA were added (change of media every 3 days). Cells were fixed on day 14. **e**, Timeline of the experiment (left) and quantification of immunofluorescence staining for $p16^{INK4a}$ (middle) and BrdU (right). IMR90 ER:RAS cells were treated with DMSO for 4 weeks, or 10 μM 3DA for 2 weeks followed by DMSO for 2 weeks, or 10 μM 3DA for 4 weeks. Media was changed every three days. Treatment was started when cells were at passage 14 and ended when cells were at passage 20. At the end of the experiment, $p16^{INK4a}$ protein expression and BrdU-positive cells were quantified. For $p16^{INK4a}$, normalized nuclear single-cell intensity values and mean of 200 cells are shown. To assess proliferation, percentage of BrdU-positive cells was measured ($n = 3$). Statistical significances were calculated using one-way ANOVA. All error bars represent mean ± s.d; *n* represents independent experiments unless otherwise stated.

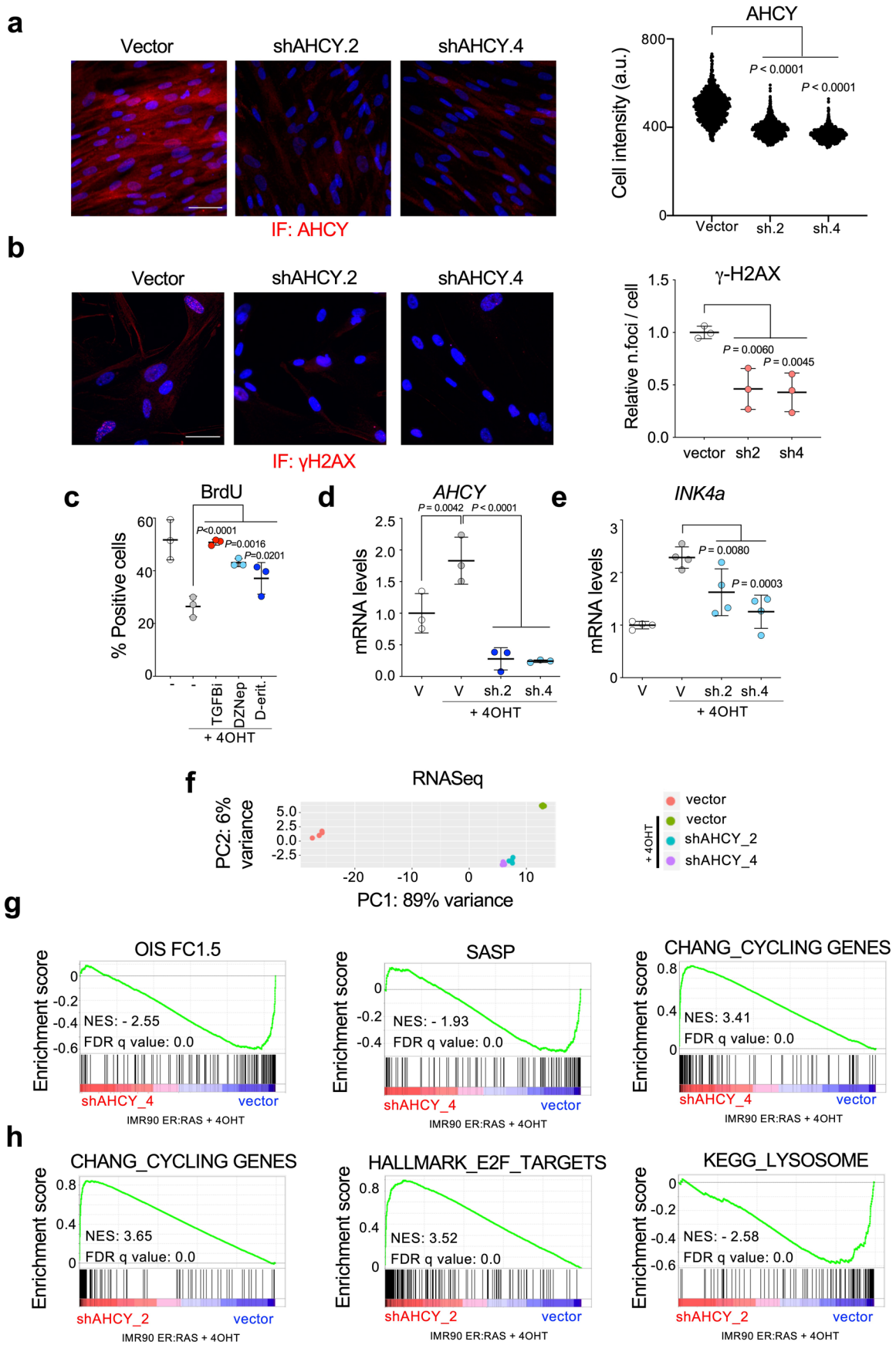

Extended Data Fig. 3 | See next page for caption.

Extended Data Fig. 3 | Genetic or chemical inhibition of AHCY alleviates oncogene-induced senescence. a, Left, representative images of immunofluorescence staining for AHCY (red). Scale bar, 50 μm. Right, single-cell intensities for AHCY ($n = 1{,}000$ cells per condition). The statistical significance was calculated using unpaired two-tailed *t*-test. **b**, Left, representative images of immunofluorescence staining for γH2AX (red). Right, quantification of immunofluorescence staining for γH2AX ($n = 4$). **c**, Quantification of immunofluorescence staining for BrdU of IMR90 ER:RAS cells four days after treatment with 4OHT or vehicle (DMSO) and 2.5 μM DZNep, 10 μM D-eritadenine and 4 μM TGF-β RI kinase inhibitor II as positive control. **d**, Expression levels of *AHCY* ($n = 4$). **e**, Expression levels of *INK4a* (encoding for $p16^{INK4a}$, $n = 4$). **f**, Principal component analysis (PCA) for the experiment described in Fig. 3f. **g**,**h**, GSEA signatures from the same experiment. All statistical significances were calculated using one-way ANOVA. All error bars represent mean ± s.d; *n* represents independent experiments unless otherwise stated.

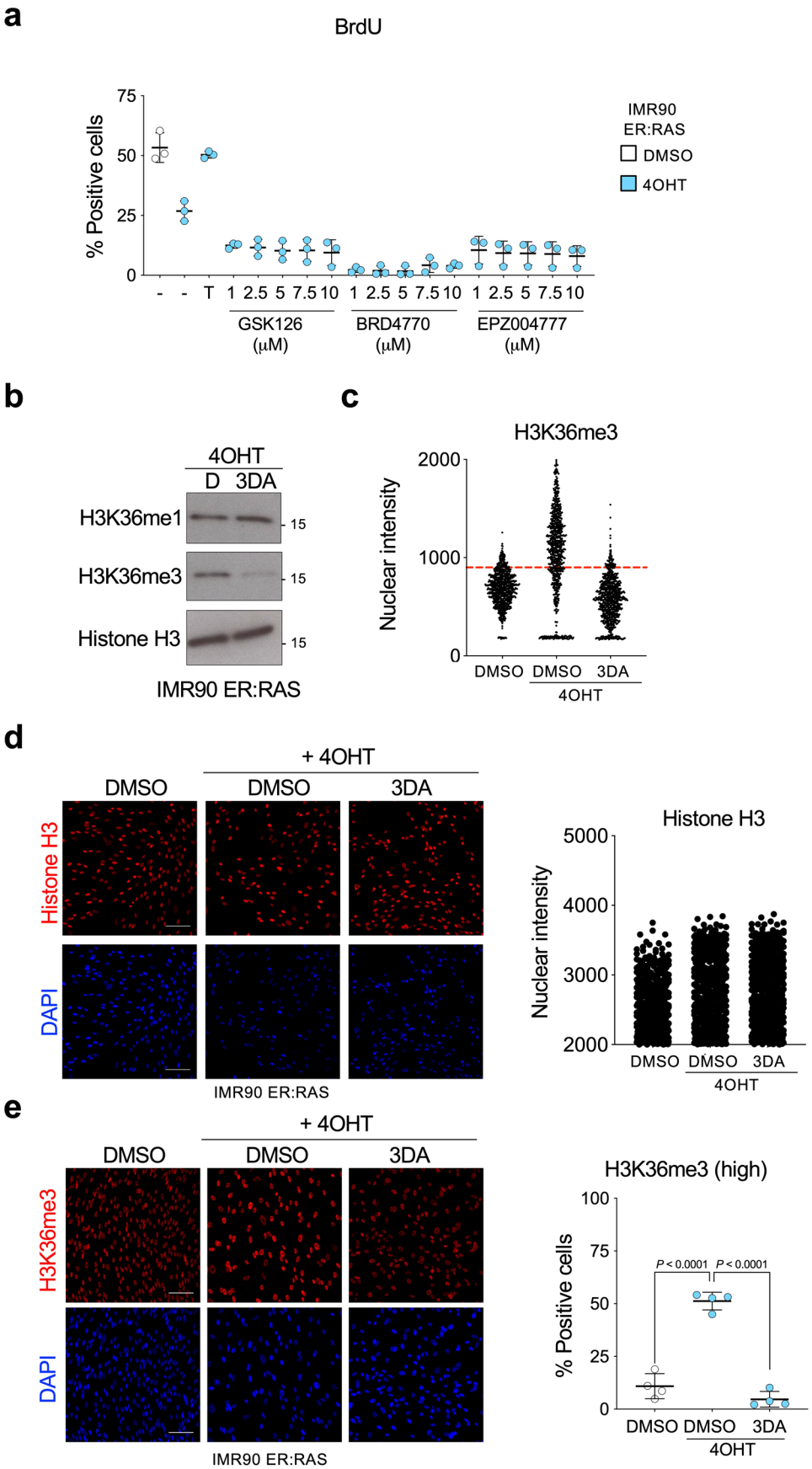

Extended Data Fig. 4 | See next page for caption.

Extended Data Fig. 4 | Contribution of histone methyltransferases and H3K36 methylation to senescence induction. a, Quantification of immunofluorescence staining for BrdU of IMR90 ER:RAS cells 4 days after treatment with 4OHT or vehicle (DMSO) and increasing concentrations of GSK126 (an inhibitor of the H3K27 methylase EZH2), BRD4770 (an inhibitor of the H3 K9 methylase EHMT2) or EPZ004777 (an inhibitor of the H3 K79 methylase DOT1L). T, 4 μM TGF-β RI kinase inhibitor II as positive control ($n=3$). All error bars represent mean ± s.d; *n* represents independent experiments. **b**, Immunoblot of protein extracts of IMR90 ER:RAS cells after 4OHT induction and treatment with 10 μM 3DA or vehicle (DMSO). Immunoblot of Histone H3 is included as a sample processing control. Immunoblots are a representative experiment out of three. **c**, Single-cell nuclear intensity values for H3K36me3 in a representative experiment out of 5 ($n=1000$ cells per condition). The threshold used to quantify the cells stained for H3K36me3 cells in Fig. 4b, is shown as a red dashed line. **d**, Left, representative immunofluorescence images of histone H3 staining (red) 4 days after 4OHT induction and treatment with 10 μM 3DA or vehicle (DMSO). Scale bar, 100 μm. Right, single-cell nuclear intensity values for histone H3 in a representative experiment out of 3 ($n=1,000$ cells). **e**, Left, representative immunofluorescence images of H3K36me3 staining (red) 6 days after treatment with 4OHT and 10 μM 3DA or vehicle (DMSO). Scale bar, 100 μm. Right, quantification ($n=4$ independent experiments). All statistical significances were calculated using one-way ANOVA. All error bars represent mean ± s.d.

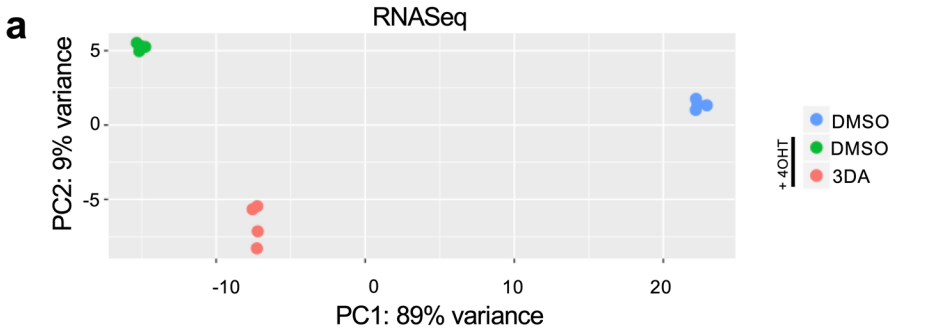

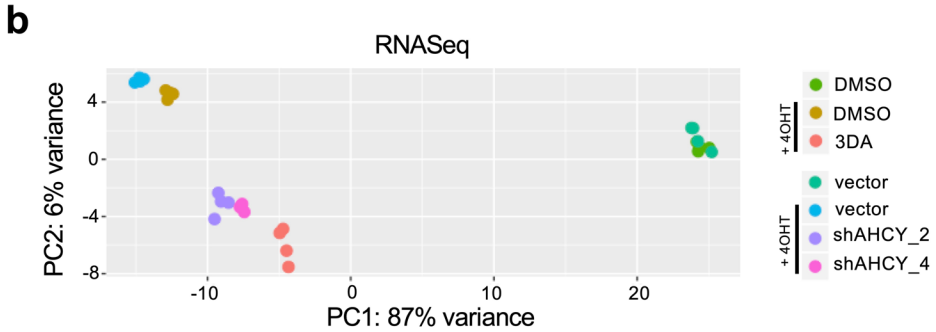

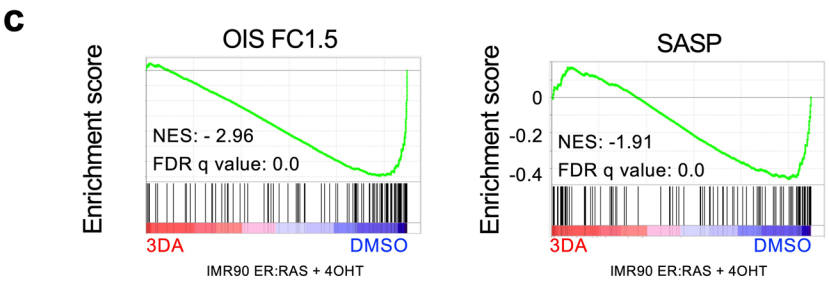

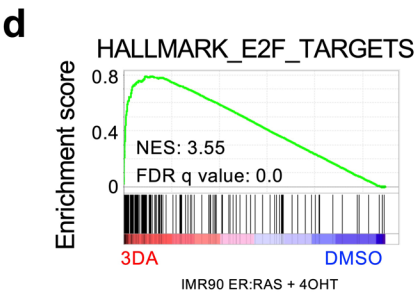

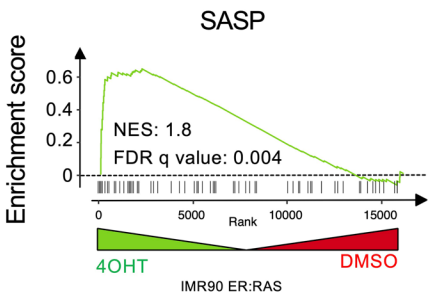

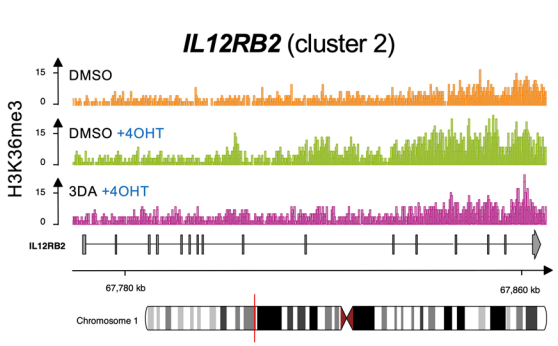

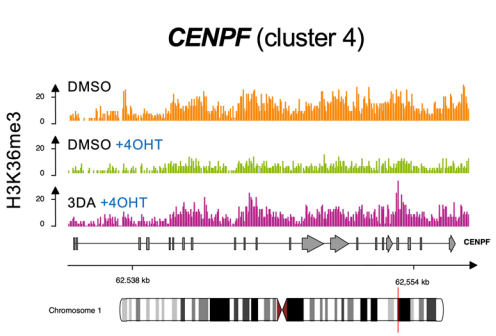

Extended Data Fig. 5 | See next page for caption.

Extended Data Fig. 5 | Transcriptional profiling after chemical or genetic inhibition of AHCY. a, Principal component analysis (PCA) for the RNASeq experiment described in Fig. 4c. **b**, Principal component analysis (PCA) including data from the experiments in Figs. 3f, 4c. **c**, GSEA of RNA-Seq data using signatures for oncogene-induced senescence and SASP. **d**, GSEA of RNA-Seq data using a signature for Hallmark E2F targets. **e**, GSEA of H3K36me3 ChIP-Seq data using a signature for SASP. **f-g**, Representative genome browser snapshots showing H3K36me3 normalized signal at *IL12RB2* (module 2, **f**) and *CENPF* (module 4, **g**) gene loci for DMSO (orange), DMSO + 4OHT (green) and 3DA + 4OHT (violet) conditions. Data are expressed as normalized counts per million reads (CPM) in 200 bp non-overlapping windows.

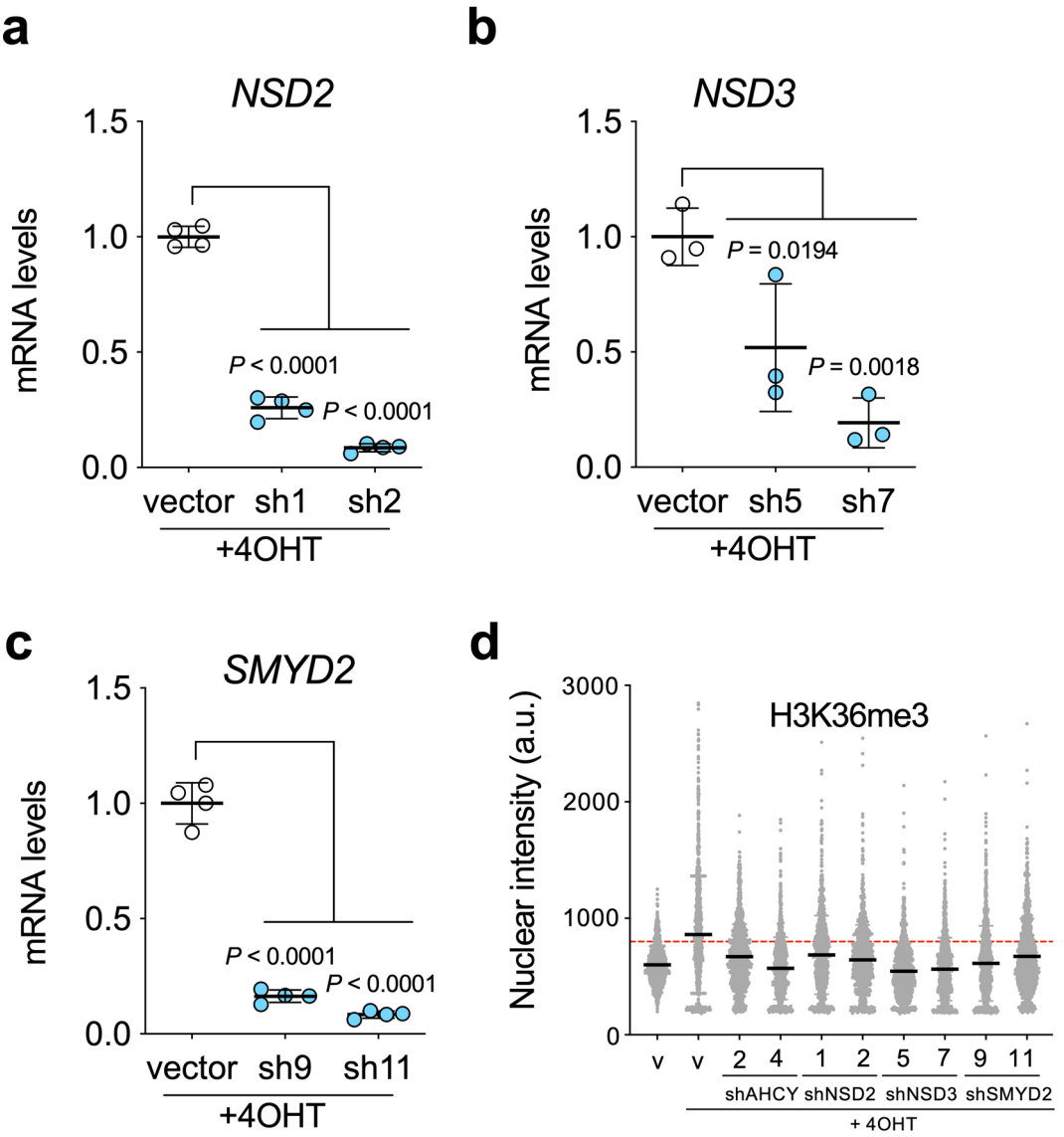

Extended Data Fig. 6 | H3K36 methylation is needed for establishing oncogene-induced senescence. a, Expression levels of *NSD2* ($n = 4$). **b**, Expression levels of *NSD3* ($n = 3$). **c**, Expression levels of *SMYD2* ($n = 4$). **d**, Single-cell nuclear intensity values for H3K36me3 staining 7 days after treatment with 4OHT or vehicle (DMSO) of IMR90 ER:RAS cells infected with different pGIPZ shRNAs against *NSD2*, *NSD3*, *SMYD2*, *AHCY* or the parental pGIPZ vector ($n = 1{,}000$ cells per condition for a representative experiment out of 3). The threshold used to quantify the cells stained for H3K36me3 cells in Fig. 5b, is shown as a red dashed line. All statistical significances were calculated using one-way ANOVA. All error bars represent mean ± s.d.

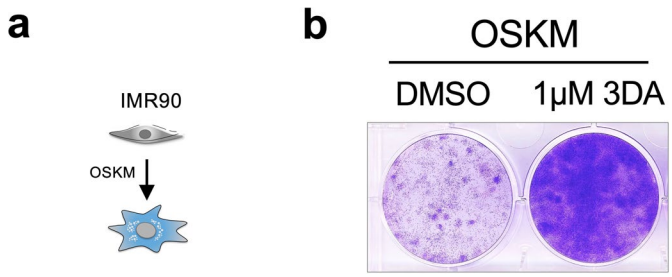

Extended Data Fig. 7 | 3-deaazadenosine inhibits reprogramming-induced senescence. a, Senescence induced in IMR90 cells upon expression of reprogramming factors (OSKM). **b**, crystal violet-stained, IMR90 cells transduced with either and empty vector or OSKM (a vector expressing reprogramming factors OCT4, SOX2, KLF4, cMYC) were treated with 1μM 3DA or vehicle (DMSO). Images are a representative experiment out of three.

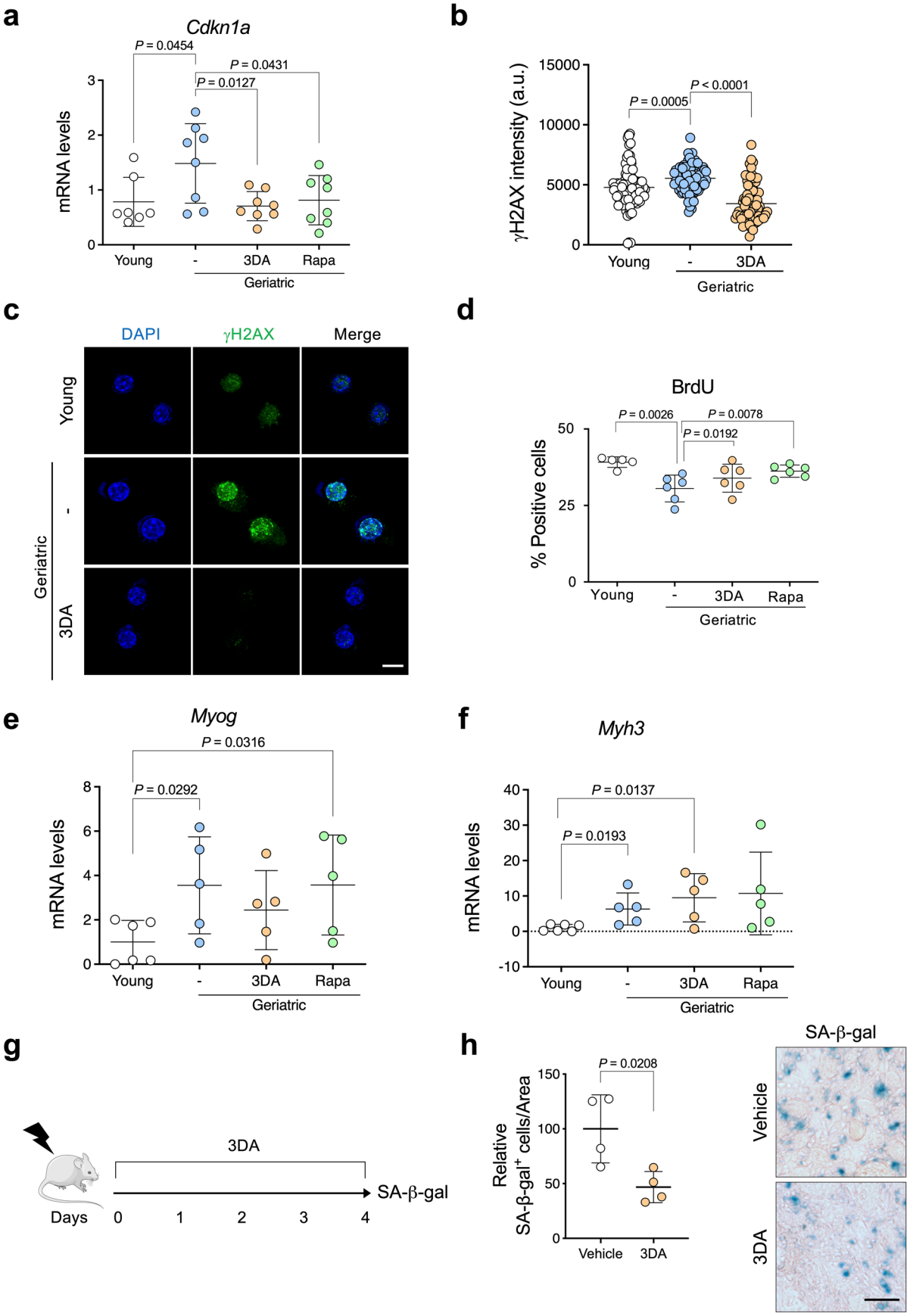

Extended Data Fig. 8 | See next page for caption.

Extended Data Fig. 8 | 3DA rejuvenates geriatric satellite cells. a-f, Analysis of the experiment described in Fig. 6a. **a**, Expression levels for mouse *Cdkn1a* mRNA (encoding for p21) in young (2–3 months, $n=7$) *versus* geriatric satellite cells (28–31 months, $n=8$). **b**, Quantification of γH2Ax intensity (arbitrary units: a.u.; $n=75$–91 cells). **c**, Representative images of γH2Ax. **d**, Quantification of BrdU staining of young (2–3 months, $n=5$) *versus* geriatric satellite cells (28–31 months, $n=7$). **e, f**, Expression levels for mouse *Myog* (**e**) and *Myh3* mRNA (**f**) in young (2–3 months, $n=6$) *versus* geriatric (28–31 months, $n=5$) satellite cells after the indicated treatments. **g**, Experimental design. Tibialis anterior muscles were injected with cardiotoxin to induce damage and regeneration. Mice were treated with vehicle or 3DA daily (10 mg/kg, i.p.) and sacrificed at 4 days post muscle injury to assess SA-β-gal activity. **h**, Left, quantification of SA- β -gal$^+$ cells in the damaged area ($n=4$ mice per group). Right, representative images of SA- β-gal staining in cryosections of tibialis anterior muscle. Scale bars 10 μm in **c** and 50 μm in **h**. All error bars represent mean ± s.d; *n* represents number of mice unless otherwise stated. Statistical significances were calculated using two-tailed unpaired *t* test. This figure was partly generated using Servier Medical Art, provided by Servier, licensed under a Creative Commons Attribution 3.0 unported license.

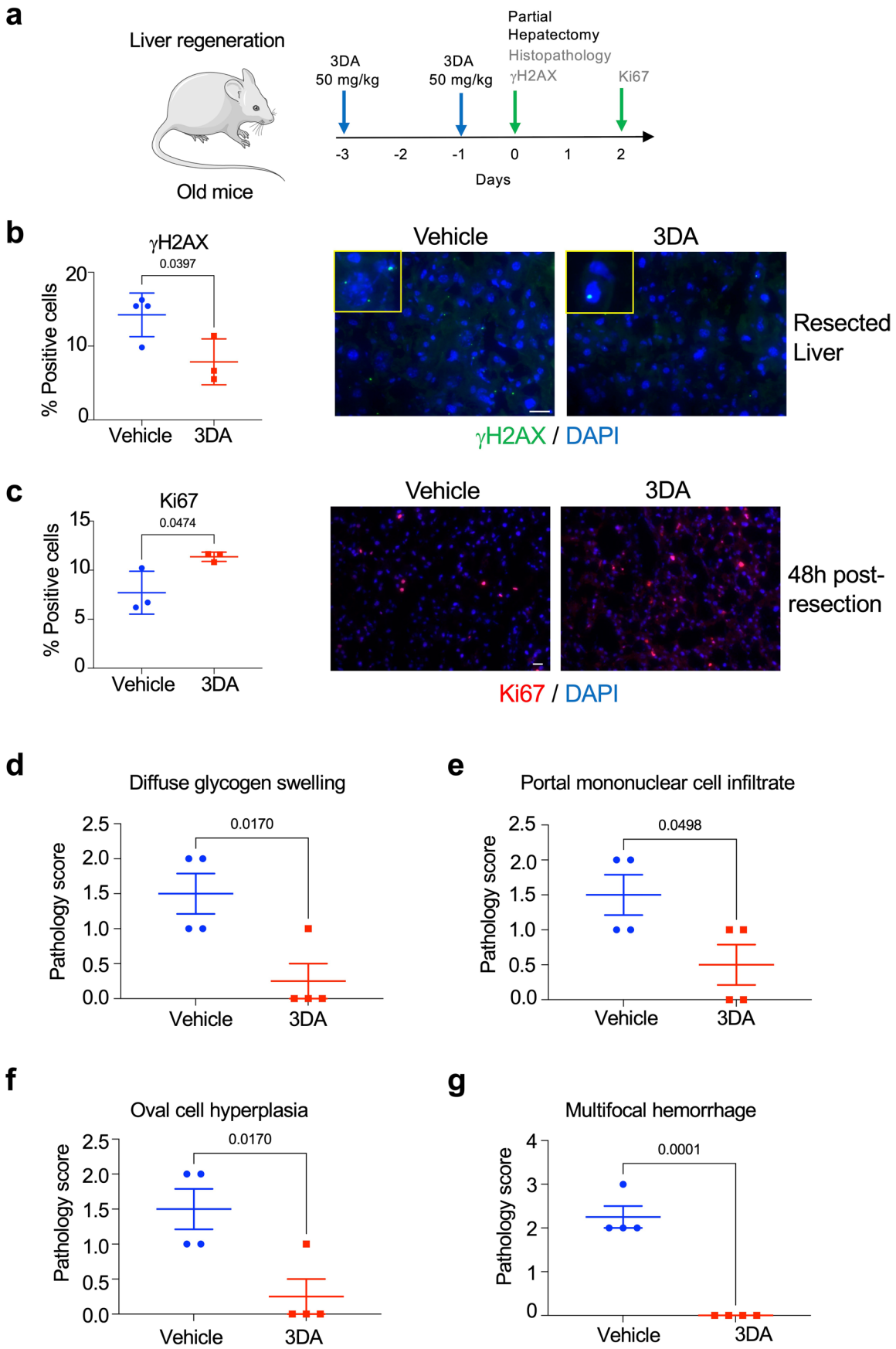

Extended Data Fig. 9 | See next page for caption.

Extended Data Fig. 9 | 3DA treatment improves liver regeneration in aged mice. a, Schematic representation of the experiment. Two-year old mice were treated 3 and 1 days before partial hepatectomy (PH) with 3DA or vehicle. The resected liver material was used for γH2AX staining and histopathology. 48 h post PH, the rest of the liver was harvested and proliferation level was determined by Ki67 staining. **b**, Right side shows representative photographs of IF staining with antibody against γH2AX and fluorescent DNA stain (DAPI). The inlay shows a magnification of positive nuclei from the respective main photograph. Left side shows the quantification. A significantly higher amount ($p < 0.05$) of γH2AX positive hepatocytes was detected in the control group (vehicle, $n = 4$) compared to experiment (3DA, $n = 3$), indicating a reduction in senescent cells. **c**, Right side shows representative photographs of IF staining with antibody against Ki67 and fluorescent DNA stain (DAPI). Left side shows the quantification. A significantly higher amount ($p < 0.05$) of Ki67 positive hepatocytes were detected in experimental group (3DA, $n = 3$) compared to control (vehicle, $n = 3$), indicating that a reduction in senescent hepatocytes is associated with improved proliferation. Statistical significance was calculated using the unpaired two-tailed Student's *t* test. Error bars are represented as mean ± SEM; *n* represents number of mice. **d-g**, Pathological score (quantified blindly in a scale from 0–5) for the indicated parameters were assigned to H&E-stained liver sections from the experimental group (3DA, $n = 4$) and control group (vehicle, $n = 4$). Statistical significance was calculated using the unpaired two-tailed Student's *t* test. Error bars are represented as mean ± SEM; *n* represents number of mice. This figure was partly generated using Servier Medical Art, provided by Servier, licensed under a Creative Commons Attribution 3.0 unported license.

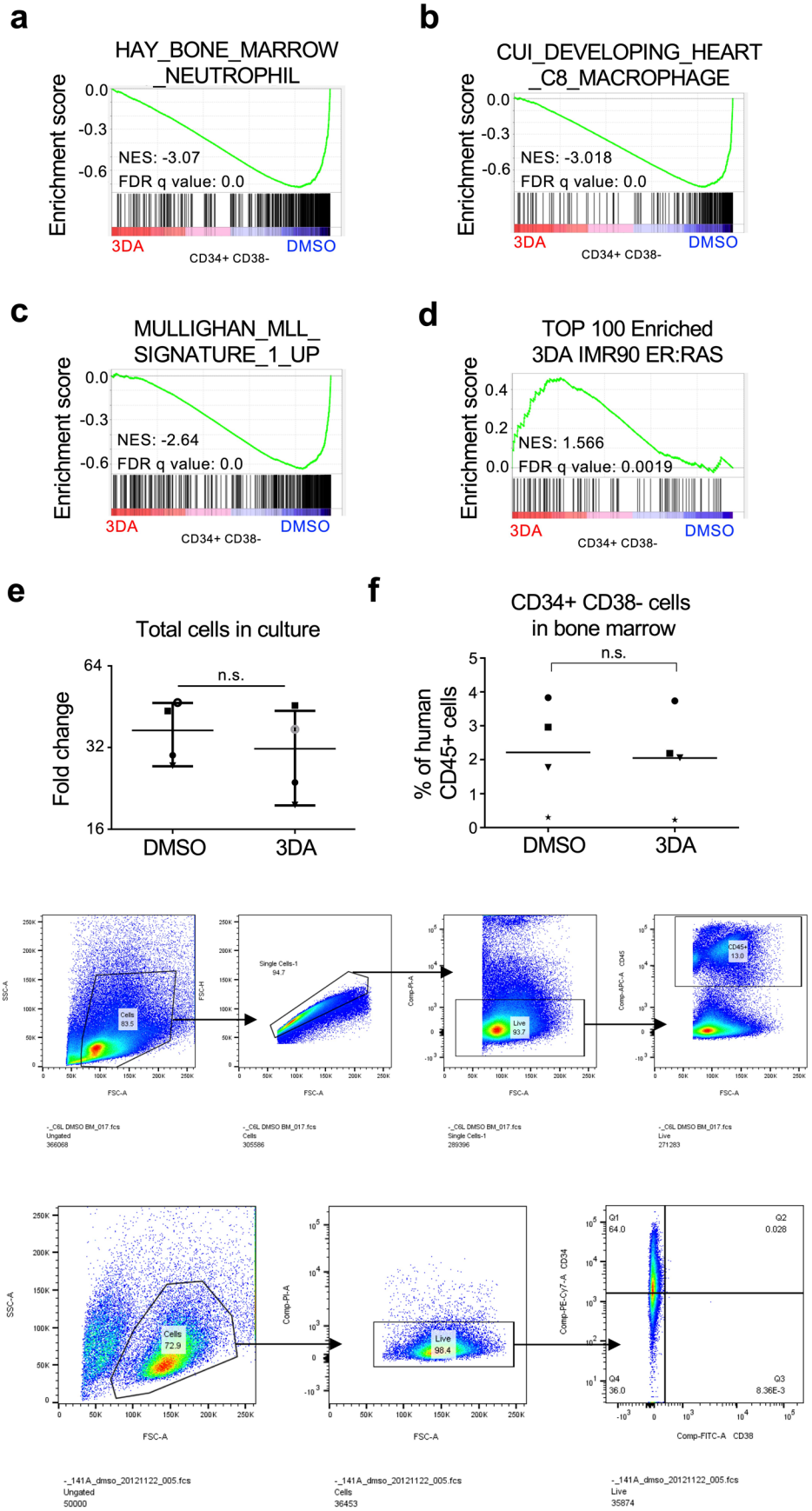

Extended Data Fig. 10 | See next page for caption.

Extended Data Fig. 10 | 3DA improves the engraftment of umbilical cord blood cells. a-**d**, GSEA signatures for the cord blood RNA-seq experiment. **e**, Cord blood-derived human hematopoietic stem and progenitor (CD34 +) cells were treated at day 1, 4 and 7 with 10 μM 3DA or DMSO and analyzed before xenotransplantation at day nine. Absolute cell numbers were determined by manual cell counting. Data are represented as mean ± SD, $n = 4$ independent experiments. Statistical significance was calculated using one-tailed Student's *t* test. **f**, 1.5×10^6 Cells from the experiment described in **a** were transplanted into NSG mice. The engraftment of human (CD45+) cells and the percentage of primitive cells (CD34 + CD38−) in the bone marrow was analyzed by flow cytometry. For **e** and **f**, each shape (open cicle, closed circle, star, square or triangle) represents a different cord blood sample. Each shape is the average of 2-3 transplanted mice with that cord blood sample ($n = 4$ independent cord blood samples). Statistical significance was calculated using one-tailed Student's *t* test. **g**, Gating strategy for the experiment shown in Fig. 7f. **h**, Gating strategy for the experiment shown in Fig. 7g.

nature research

Corresponding author(s): JESUS GIL

Last updated by author(s): Aug 3, 2022

Reporting Summary

Nature Research wishes to improve the reproducibility of the work that we publish. This form provides structure for consistency and transparency in reporting. For further information on Nature Research policies, see our Editorial Policies and the Editorial Policy Checklist.

Statistics

For all statistical analyses, confirm that the following items are present in the figure legend, table legend, main text, or Methods section.

n/a	Confirmed	
☐	☒	The exact sample size (*n*) for each experimental group/condition, given as a discrete number and unit of measurement
☐	☒	A statement on whether measurements were taken from distinct samples or whether the same sample was measured repeatedly
☐	☒	The statistical test(s) used AND whether they are one- or two-sided *Only common tests should be described solely by name; describe more complex techniques in the Methods section.*
☒	☐	A description of all covariates tested
☐	☒	A description of any assumptions or corrections, such as tests of normality and adjustment for multiple comparisons
☐	☒	A full description of the statistical parameters including central tendency (e.g. means) or other basic estimates (e.g. regression coefficient) AND variation (e.g. standard deviation) or associated estimates of uncertainty (e.g. confidence intervals)
☐	☒	For null hypothesis testing, the test statistic (e.g. *F*, *t*, *r*) with confidence intervals, effect sizes, degrees of freedom and *P* value noted *Give P values as exact values whenever suitable.*
☒	☐	For Bayesian analysis, information on the choice of priors and Markov chain Monte Carlo settings
☒	☐	For hierarchical and complex designs, identification of the appropriate level for tests and full reporting of outcomes
☒	☐	Estimates of effect sizes (e.g. Cohen's *d*, Pearson's *r*), indicating how they were calculated

Our web collection on statistics for biologists contains articles on many of the points above.

Software and code

Policy information about availability of computer code

Data collection	IN Cell Analyzer 2000 version 5.2-14311 (64-bit) GE Healthcare. Zeiss LSM software Zen 2 Blue.
Data analysis	GraphPad Prism 8 (version 8.1.2) for macOS High Sierra was used for statistical analysis. IN Cell Investigator 1000 workstation 3.7.2, build 1860. ImageJ 2.0.0-rc-54/1.51g. ELDA software (Hu & Smyth, 2009) (online available at: https://bioinf.wehi.edu.au/software/elda/, version 24 October 2014). FlowJo (version 7). Tophat v2.0.11. HTSeq v0.5.3p9. DESeq2 1.30.1 GSEA v2.07 (Broad Institute). ea-utils suite v1.1.2 bowtie v1.1.1 samtools v1.2 PicardTools v1.130 spp v1.10.1 MACS v2.1.0 preseqR 3.1.2 DiffBind package 2.16.2 EDASeq package 2.22.0 RUVSeq package 1.22.0

edgeR 3.30.3
Ensembl v86.
Rsubread package 2.2.6
R (R Foundation for Statistical Computing, Vienna, Austria).
Real Time Analysis (RTA) v2.11.3
NextSeq 500 Control software v4.0.2
CASAVA-2.17

For manuscripts utilizing custom algorithms or software that are central to the research but not yet described in published literature, software must be made available to editors and reviewers. We strongly encourage code deposition in a community repository (e.g. GitHub). See the Nature Research guidelines for submitting code & software for further information.

Data

Policy information about availability of data

All manuscripts must include a data availability statement. This statement should provide the following information, where applicable:

- Accession codes, unique identifiers, or web links for publicly available datasets
- A list of figures that have associated raw data
- A description of any restrictions on data availability

Source data is included with this paper. The RNA-seq and ChIP-seq data generated in the present study have been deposited in the Gene Expression Omnibus database under accession numbers GSE155906 and GSE175770.

Field-specific reporting

Please select the one below that is the best fit for your research. If you are not sure, read the appropriate sections before making your selection.

☒ Life sciences ☐ Behavioural & social sciences ☐ Ecological, evolutionary & environmental sciences

For a reference copy of the document with all sections, see nature.com/documents/nr-reporting-summary-flat.pdf

Life sciences study design

All studies must disclose on these points even when the disclosure is negative.

Sample size	No statistical methods were used to pre-determine sample sizes, but our sample sizes are similar to those reported previously (Jung et al. Cell Reports, 2019; Sousa-Victor et al. Nature, 2014; Garcia-Prat et al. 2016, Nature; Loforese et al. EMBO Molecular Medicine, 2017).
Data exclusions	Mice with engraftment <1% were not included in further analysis in the cord blood experiment. In the liver regeneration experiment, mice which died upon operation could not be analysed at day 2. There were also technical issues with the frozen sections of a treated mice at day 0 and it was excluded for the gH2AX analysis.
Replication	All experiments were reproducible. Every figure states how many times each experiment was performed with similar results.
Randomization	The in vivo studies, with mouse satellite cells were not randomized. For the liver regeneration experiments, All animals were randomly allocated into carrier (n = 4) or treatment (n = 4) group. For the cord blood xenotransplantations, recipient mice were randomly assigned to an experimental group. Cell culture experiments did not require randomisation because the tests were compared to controls. Plates needed to be marked to ensure the treatments are delivered to the appropriate plates (and not the control) and randomisation would not be practical or feasible.
Blinding	Investigators were not blinded to allocation and outcome assessment for the satellite cell transplantation experiment, as engraftment of both conditions was performed within the same host mice. Investigators were not blinded during data collection after the xenotransplantation of cord blood cells. For the liver regeneration experiment, staining and counting were done in a blinded fashion, the person was not aware to which group the animal belonged. Investigators were not blinded during the cell culture experiments.

Reporting for specific materials, systems and methods

We require information from authors about some types of materials, experimental systems and methods used in many studies. Here, indicate whether each material, system or method listed is relevant to your study. If you are not sure if a list item applies to your research, read the appropriate section before selecting a response.

Materials & experimental systems

n/a	Involved in the study
☐	☒ Antibodies
☐	☒ Eukaryotic cell lines
☒	☐ Palaeontology and archaeology
☐	☒ Animals and other organisms
☐	☒ Human research participants
☒	☐ Clinical data
☒	☐ Dual use research of concern

Methods

n/a	Involved in the study
☐	☒ ChIP-seq
☐	☒ Flow cytometry
☒	☐ MRI-based neuroimaging

Antibodies

Antibodies used

The following primary antibodies were used in this study: rat monoclonal anti-BrdU (BU1/75(ICR1); Abcam, ab6326) 1:2000, mouse monoclonal anti-p16INK4a (JC-8; from CRUK) 1:1000, rabbit polyclonal anti-p21 (M-19; Santa Cruz, sc-471) 1:200, mouse monoclonal anti-SAHH (A-11; Santa Cruz, sc-271389) 1:100, rabbit anti-phospho-histone H2A.X (Ser139) (Cell Signaling Technology, 2577) 1:50, mouse monoclonal anti- phospho-histone H2A.X (Ser139) (3F2; Thermo Fischer Scientific, MA1-2022) 1:250, rabbit polyclonal anti-Ki67 (Abcam, ab15580) 1:200, rabbit polyclonal anti-53BP1 (Novus Biologicals, NB100-304) 1:1000, rabbit monoclonal anti-Mono-Methyl-Histone H3 (Lys36) (D9J1D, Cell Signaling Technology, 14111) 1:1000, rabbit monoclonal anti-Tri-Methyl-Histone H3 (Lys36) (D5A7, Cell Signaling Technology, 4909) 1:1000, rabbit monoclonal anti-Tri-Methyl-Histone H3 (Lys4) (C42D8; Cell Signaling Technology, 9751) 1:1000, rabbit monoclonal anti-Tri-Methyl-Histone H3 (Lys9) (D4W1U; Cell Signaling Technology, 13969) 1:1000, rabbit monoclonal anti-Tri-Methyl-Histone H3 (Lys27) (C36B11; Cell Signaling Technology, 9733) 1:1000, rabbit polyclonal anti-Tri-Methyl-Histone H3 (Lys79) (Cell Signaling Technology, 4260) 1:1000, rabbit polyclonal anti-H3 (Abcam, ab1791) 1:5000, and rabbit polyclonal anti-GFP (Invitrogen, A6455) 1:400. We used the following secondary antibodies: goat anti-mouse IgG (H+L) AlexaFluor 594 conjugated (Thermo Fischer Scientific, A11032) 1:500, goat anti-rat IgG (H+L) AlexaFluor488 conjugated (Thermo Fischer Scientific, A11006) 1:500, goat anti-rabbit IgG-HRP (Santa Cruz, sc-2004) 1:5000, and biotinylated goat anti-rat antibody (712-066-150 Jackson Immunoresearch) 1:250.

Validation

BrdU
https://www.abcam.com/brdu-antibody-bu175-icr1-proliferation-marker-ab6326.html
p16INK4a (JC-8)
https://www.scbt.com/p/p16-antibody-jc8
p21
https://www.scbt.com/p/p21-antibody-m-19
SAHH
https://www.scbt.com/p/sahh-antibody-a-11
Phospho-histone H2A.X
https://www.cellsignal.co.uk/products/primary-antibodies/phospho-histone-h2a-x-ser139-antibody/2577
Phospho-histone H2A.X (3F2)
https://www.thermofisher.com/antibody/product/Phospho-Histone-H2A-X-Ser139-Antibody-clone-3F2-Monoclonal/MA1-2022
Ki67
https://www.abcam.com/ki67-antibody-ab15580.html
53BP1
https://www.novusbio.com/products/53bp1-antibody_nb100-304
H3K36me1
https://www.cellsignal.co.uk/products/primary-antibodies/mono-methyl-histone-h3-lys36-d9j1d-rabbit-mab/14111
H3K36me3
https://www.cellsignal.co.uk/products/primary-antibodies/tri-methyl-histone-h3-lys36-d5a7-xp-rabbit-mab/4909
Try-Methyl Histone 3 antibody sampler kit
https://www.cellsignal.co.uk/products/primary-antibodies/tri-methyl-histone-h3-antibody-sampler-kit/9783
H3
https://www.abcam.com/histone-h3-antibody-nuclear-marker-and-chip-grade-ab1791.html
GFP
https://www.thermofisher.com/antibody/product/GFP-Antibody-Polyclonal/A-6455

Eukaryotic cell lines

Policy information about cell lines

Cell line source(s)	HEK-293T and IMR-90 cells were obtained from ATCC. MS-5 cells were obtained from DSMZ.
Authentication	Human cell lines were authenticated by DNA (STR) profile performed by Eurofins. MS-5 were not authenticated.
Mycoplasma contamination	All cell lines were routinely tested for mycoplasma contamination and were negative.
Commonly misidentified lines (See ICLAC register)	None of the cell lines used in this study is present in the database of commonly misidentified cell lines.

Animals and other organisms

Policy information about studies involving animals; ARRIVE guidelines recommended for reporting animal research

Laboratory animals	For the muscle satellite experiments, C57Bl/6 (WT) mice were bred and aged at the animal facility of the Barcelona Biomedical Research Park (PRBB), housed in standard cages under 12-hour light-dark cycles and fed ad libitum with a standard chow diet. Mouse stem cells were isolated from young (2-3 months old) or geriatric (28-31 months) male C57BL/6 wild-type mice. For the liver regeneration experiments, 6-month-old female C57BL/6JInv mice were purchased from InVivos and further kept until 2-year-old. Mice were housed in BRC in SPF conditions under a 12 hour light / dark cycle with lights turn off at 7 pm and resume at 7 am. The animals were housed in individually ventilated cages with their temperature and humidity maintained at ~21ºC and 60-65% rH. Two-thirds (partial) hepatectomy (2/3 PH) was performed on 2-year-old C57Bl6/J wild type mice For cord blood xenotransplant experiments, female 10-25 weeks old NOD.Cg-Prkdcscid Il2rgtm1Wjl/SzJ mice were used. Mice were kept in sterile conditions in individually ventilated filter-top cages at 20o C under 12 hours dark/light cycles.
Wild animals	No wild animals were used in this study.
Field-collected samples	This study did not involve samples collected in the field.
Ethics oversight	Mouse experiments were performed in line with international and national guidelines. Isolation of mouse stem cells for ex vivo culture was approved by the ethics committee of the (Barcelona Biomedical Research Park (PRBB) and by the Catalan Government (Spain) and used sex-, age- and weight-matched littermate animals. Mouse liver regeneration experiments were approved by the A*STAR BRC (Biological Resource Centre) IACUC committee, IACUC protocol#: 191452 (Title of project: Identification of liver disease intervention points and enhancing liver regeneration). Xenotransplants experiments were approved by the Institutional Animal Care and Use Committee of the University of Groningen (IACUC-RUG).

Note that full information on the approval of the study protocol must also be provided in the manuscript.

Human research participants

Policy information about studies involving human research participants

Population characteristics	Human cord blood from healthy full-term pregnancies.
Recruitment	Human cord blood was acquired from healthy full-term pregnancies delivered at the Obstetrics department at the Isala Hospital in Zwolle (The Netherlands) after informed consent was provided by pregnant mothers, in accordance with the Declaration of Helsinki. No compensation was offered. Only cord blood samples were sufficient volume was obtained were further processed.
Ethics oversight	Medisch Ethisch Toetsings Commissie (METC) of Isala Hospital Zwolle.

Note that full information on the approval of the study protocol must also be provided in the manuscript.

ChIP-seq

Data deposition

☒ Confirm that both raw and final processed data have been deposited in a public database such as GEO.

☒ Confirm that you have deposited or provided access to graph files (e.g. BED files) for the called peaks.

Data access links *May remain private before publication.*	The RNA-seq and ChIP-seq data generated in the present study have been deposited in the Gene Expression Omnibus database under accession number GSE155906. It can be accessed via the following private link (use token anwfwoymzzyjpkx).
Files in database submission	GSE155903 - Analysis of the senescent transcriptome after treatment with 3-deazaadenosine. GSE155904 - Analysis of the senescent transcriptome after knockdown of AHCY. GSE155905 - Effect of 3-deazaadenosine on the H3K36me3 chromatin landscape during senescence (ChIP-seq).
Genome browser session (e.g. UCSC)	https://www.ncbi.nlm.nih.gov/geo/query/acc.cgi?acc=GSE155906

Methodology

Replicates	Two replicates for each of the following treatments: input-DMSO Input-4OHT Input-3DA H3K36me3-DMSO H3K36me3-4OHT H3K36me3-3DA
Sequencing depth	Total number of reads: 30-50 million;

Sequencing depth	Uniquely mapped reads: Length of read: > 25bp after filtering. Single-end.
Antibodies	Rabbit monoclonal anti-Tri-Methyl Histone H3 (Lys36) (D5A7, Cell Signaling Technology, 4909). Rabbit polyclonal anti-H3 (Abcam, ab1791).
Peak calling parameters	Peak calling (NOTE : the IDR pipeline is not detailed here) : macs2 callpeak --tempdir ./ -t in_chip.bam -c in_control.bam --name out --nomodel --extsize 100 --gsize mm -p 1e-1
Data quality	Read filtering and trimming : fastq-mcf -C 500000 -q 30 -l 25 -S --qual-mean 30 -max-ns 1 -o out.fastq ILLUMINA_PRIMER_INDEX_N.fasta in.fastq Alignments with best-match parameters : bowtie -v 2 -m 1 --best --strata --S mm10.fa in.fastq | samtools view -Sb - > out.bam Sort aligments : samtools sort in.bam -o out.bam -T in.tmp Remove PCR / optical duplicates : java -jar picard.jar MarkDuplicates REMOVE_DUPLICATES=FALSE METRICS_FILE=out.txt INPUT=in.bam OUTPUT=out.bam samtools view -h -F 0x400 in.bam | samtools view -hSb - -o out.bam Remove alignments in Encode blacklisted regions : intersectBed -v -abam in.bam -b encode_blacklist.bed > out.bam Compute the average fragments length : Rscript run_spp_nodups.R -rf -c=in.bam -odir=./ -savp=out.pdf -out=out.txt -s=-100:5:1500 -x=-500:85
Software	eautils v1.1.2 fastqscreen v0.4.4 bowtie v1.1.1 samtools v1.2 picardtools v1.130 bedtools 2.19.1 spp v1.10.1 macs v2.1.0 idr v1.0 deepTools v2.4.2

Flow Cytometry

Plots

Confirm that:

☒ The axis labels state the marker and fluorochrome used (e.g. CD4-FITC).

☒ The axis scales are clearly visible. Include numbers along axes only for bottom left plot of group (a 'group' is an analysis of identical markers).

☒ All plots are contour plots with outliers or pseudocolor plots.

☒ A numerical value for number of cells or percentage (with statistics) is provided.

Methodology

Sample preparation	Cord blood-derived HSPCs were cultured in Stemspan (Stem Cell Technologies) supplemented with 1% v/v penicillin-streptomycin-glutamine (100X) (Gibco) and the cytokines FLT3L, TPO and SCF (R&D Systems), all at a concentration of 100ng/mL. The cells were seeded at a starting density of 250.000 cells/mL and treated with 10 µM 3DA or vehicle (DMSO) at days 1, 4, and 7. Cells were cultured in a humidified atmosphere of 5% CO2 at 37°C. Cells were harvested and counted manually with a hemocytometer and trypan blue at day 9. These cells were analyzed by FACS and used for RNA-seq and xenotransplantation.
Instrument	FACSCanto II (BD) and LSR II (BD).
Software	FlowJo (version 7).
Cell population abundance	We did not sort cells by flow, but CD34+ cells were isolated using MACS.

Gating strategy	Dead cells were excluded from the analysis by gating out lower forward scatter and high DAPI or propidium iodide-retaining cells.

☒ Tick this box to confirm that a figure exemplifying the gating strategy is provided in the Supplementary Information.